

000 001 002 003 004 005 006 007 008 009 010 011 012 013 014 015 016 017 018 019 020 021 022 023 024 025 026 027 028 029 030 031 032 033 034 035 036 037 038 039 040 041 042 043 044 045 046 047 048 049 050 051 052 053 AREUREDI: ANNEALED RECTIFIED UPDATES FOR REFINING DISCRETE FLOWS WITH MULTI-OBJECTIVE GUIDANCE

006
007 **Anonymous authors**
008 Paper under double-blind review

010 ABSTRACT

012 Designing sequences that satisfy multiple, often conflicting, objectives is a cen-
013 tral challenge in therapeutic and biomolecular engineering. Existing generative
014 frameworks largely operate in continuous spaces with single-objective guidance,
015 while discrete approaches lack guarantees for multi-objective Pareto optimality. We
016 introduce **AReUREDi** (Annealed Rectified Updates for Refining Discrete Flows),
017 a discrete optimization algorithm with theoretical guarantees of convergence to the
018 Pareto front. Building on Rectified Discrete Flows (ReDi), AReUREDi combines
019 Tchebycheff scalarization, locally balanced proposals, and annealed Metropolis-
020 Hastings updates to bias sampling toward Pareto-optimal states while preserv-
021 ing distributional invariance. Applied to peptide and SMILES sequence design,
022 AReUREDi simultaneously optimizes up to five therapeutic properties (including
023 affinity, solubility, hemolysis, half-life, and non-fouling) and outperforms both
024 evolutionary and diffusion-based baselines. These results establish AReUREDi as
025 a powerful, sequence-based framework for multi-property biomolecule generation.

026 1 INTRODUCTION

028 The design of biological sequences must account for multiple, often conflicting, objectives (Naseri
029 & Koffas, 2020). Therapeutic molecules, for example, must combine high binding affinity with
030 low immunogenicity and favorable pharmacokinetics (Tominaga et al., 2024); CRISPR guide RNAs
031 require both high on-target activity and minimal off-target effects (Mohr et al., 2016; Schmidt
032 et al., 2025); and synthetic promoters must deliver strong expression while remaining tissue-specific
033 (Artemyev et al., 2024). These examples illustrate that biomolecular engineering is inherently a
034 multi-objective optimization problem.

035 Yet, most computational frameworks continue to optimize single objectives in isolation (Zhou et al.,
036 2019; Nehdi et al., 2020; Nisonoff et al., 2025). While such approaches can reduce toxicity (Kreiser
037 et al., 2020; Sharma et al., 2022) or improve thermostability (Komp et al., 2025), they often create
038 adverse trade-offs: high-affinity peptides may be insoluble or hemolytic, and stabilized proteins may
039 lose specificity (Bigi et al., 2023; Rinauro et al., 2024). Black-box multi-objective optimization
040 (MOO) methods such as evolutionary search and Bayesian optimization have long been applied to
041 molecular design (Zitzler & Thiele, 1998; Deb, 2011; Ueno et al., 2016; Frisby & Langmead, 2021),
042 but these approaches scale poorly in high-dimensional sequence spaces.

043 To overcome this, recent generative approaches have incorporated controllable multi-objective
044 sampling (Li et al., 2018; Sousa et al., 2021; Yao et al., 2024). For instance, ParetoFlow (Yuan
045 et al., 2024) leverages continuous-space flow matching to generate Pareto-optimal samples. However,
046 extending such guarantees to biological sequences is challenging, since discrete data typically require
047 embedding into continuous manifolds, which distorts token-level structure and complicates property-
048 based guidance (Beliakov & Lim, 2007; Michael et al., 2024).

049 A more direct path lies in discrete flow models (Campbell et al., 2024; Gat et al., 2024; Dunn &
050 Koes, 2024). These models define probability paths over categorical state spaces, either through
051 simplex-based interpolations (Stark et al., 2024; Davis et al., 2024; Tang et al., 2025a) or jump-process
052 flows that learn token-level transition rates (Campbell et al., 2024; Gat et al., 2024). Recent advances
053 have shown their promise for controllable single-objective generation (Nisonoff et al., 2025; Tang
et al., 2025a), but no framework yet achieves Pareto guidance across multiple objectives.

054 Here, the notion of rectification provides a crucial building block. In the continuous setting, *Rectified*
 055 *Flows* (Liu et al., 2023) learn to straighten ODE paths between distributions, thereby reducing convex
 056 transport costs and enabling efficient few-step or even one-step sampling. Recently, **ReDi** (*Rectified*
 057 *Discrete Flows*) (Yoo et al., 2025) extended this principle to discrete domains. By iteratively refining
 058 the coupling between source and target distributions, ReDi provably reduces factorization error
 059 (quantified as conditional total correlation) while maintaining distributional fidelity. This makes
 060 ReDi highly effective for efficient discrete sequence generation. However, ReDi does not address
 061 the multi-objective setting, as it lacks a mechanism to steer sampling toward the *Pareto front*, where
 062 improvements in one objective cannot be made without degrading another. This is a critical limitation
 063 for biomolecular design, where trade-offs define practical success.

064 To address this, we introduce **AReUReDi** (Annealed **R**ectified **U**pdates for **R**efining **D**iscrete **F**lows),
 065 a new framework that extends rectified discrete flows with multi-objective guidance. AReUReDi
 066 integrates three innovations: (i) *annealed Tchebycheff scalarization*, which gradually sharpens the
 067 focus on balanced solutions across objectives (Lin et al., 2024a); (ii) *locally balanced proposals*, which
 068 combine the generative prior of ReDi with multi-objective guidance while ensuring reversibility;
 069 and (iii) *Metropolis-Hastings updates*, which preserve exact distributional invariance and guarantee
 070 convergence to Pareto-optimal states. Together, these mechanisms refine rectified discrete flows into
 071 a principled Pareto sampler.

072 Our key contributions are:

- 074 1. We propose AReUReDi, the first multi-objective extension of rectified discrete flows, integrating
 075 annealed scalarization, locally balanced proposals, and MCMC updates.
- 076 2. We provide theoretical guarantees that AReUReDi preserves distributional invariance and
 077 converges to the Pareto front with full coverage.
- 078 3. We demonstrate that AReUReDi can optimize up to five competing biological properties
 079 simultaneously, including affinity, solubility, hemolysis, half-life, and non-fouling.
- 080 4. We benchmark AReUReDi against classical MOO algorithms and state-of-the-art discrete
 081 diffusion approaches, showing superior trade-off navigation and biologically plausible sequence
 082 designs.

085 2 PRELIMINARIES

087 2.1 DISCRETE FLOW MATCHING

089 Let $\mathcal{S} = V^L$ denote the discrete state space, where V is a vocabulary of size K and each $x =$
 090 $(x_1, \dots, x_L) \in \mathcal{S}$ is a sequence of tokens. A *discrete flow matching (DFM)* model (Campbell et al.,
 091 2024; Gat et al., 2024; Dunn & Koes, 2024) defines a probability path $\{p_t\}_{t \in [0,1]}$ interpolating
 092 between a simple source distribution p_0 and a target distribution p_1 by means of a coupling $\pi(x_0, x_1)$
 093 and conditional bridge distributions $p_t(x_t | x_0, x_1)$. The model is trained to approximate conditional
 094 transitions $p_{s|t}(x_s | x_t)$ for $0 \leq t < s \leq 1$.

095 Since the joint distribution over L coordinates is intractable, DFMs employ a factorization

$$097 p_{s|t}(x_s | x_t) \approx \prod_{i=1}^L p_{s|t}(x_s^i | x_t),$$

100 which introduces a discrepancy measured by the conditional total correlation

$$103 \text{TC}_{s|t} = \text{KL}\left(p_{s|t}(x_s | x_t) \middle\| \prod_{i=1}^L p_{s|t}(x_s^i | x_t)\right).$$

106 This quantity captures the inter-dimensional dependencies neglected under factorization, and grows
 107 with larger step sizes (Stark et al., 2024; Davis et al., 2024; Tang et al., 2025a). As a result, DFMs are
 accurate in the many-step regime but degrade under few-step or one-step generation.

108 2.2 RECTIFIED DISCRETE FLOW
109

110 To mitigate factorization error, **Rectified Discrete Flow (ReDi)** (Yoo et al., 2025) introduces an
111 iterative rectification of the coupling π . Starting from an initial coupling $\pi^{(0)}(x_0, x_1)$, a DFM is
112 trained under $\pi^{(k)}$ to produce new source–target pairs, defining an empirical joint distribution $\hat{\pi}^{(k)}$.
113 The coupling is then updated via

$$114 \quad \pi^{(k+1)}(x_0, x_1) \propto \pi^{(k)}(x_0, x_1) \frac{p_{\theta^{(k)}}(x_1 | x_0)}{p_{\theta^{(k)}}(x_1)},$$

116 where $p_{\theta^{(k)}}(x_1 | x_0)$ is the conditional distribution learned at iteration k . This yields a sequence of
117 couplings $\{\pi^{(k)}\}_{k \geq 0}$ with provably decreasing conditional TC,
118

$$119 \quad \text{TC}_{s|t}(\pi^{(k+1)}) \leq \text{TC}_{s|t}(\pi^{(k)}).$$

120 By progressively reducing factorization error, ReDi produces a well-calibrated base distribution p_1
121 with low inter-dimensional correlation. This base distribution provides reliable marginal transition
122 probabilities $p_t^i(\cdot | x_t)$ for each coordinate i at time t , which serve as the generative prior in the
123 AReUREDi framework. Rectification follows the same principle as *Rectified Flow* in continuous
124 domains (Liu et al., 2023), where iterative refinement straightens ODE paths and decreases transport
125 costs.

126 3 AREUREDI: ANNEALED RECTIFIED UPDATES FOR REFINING DISCRETE
127 FLOWS
128

129 With an efficient discrete flow-based generation framework in hand, we develop AReUREDi that
130 extends ReDi (Yoo et al., 2025) to the multi-objective optimization setting, where the goal is
131 to generate discrete samples that approximate the Pareto front of multiple competing objectives.
132 Starting from a pre-trained ReDi model, AReUREDi incorporates annealed guidance, locally balanced
133 proposals, and Metropolis-Hastings updates to progressively bias the sampling process toward Pareto-
134 optimal states while preserving the probabilistic guarantees of the underlying flow (Algorithm 1).
135

136 3.1 PROBLEM SETUP
137

138 Let the discrete search space be $\mathcal{S} = \mathcal{V}^L$, where \mathcal{V} is a finite vocabulary of size K and each state
139 $x = (x_1, \dots, x_L) \in \mathcal{S}$ is a sequence of tokens. We assume access to a pre-trained ReDi model that
140 provides marginal transition probabilities $p_t^i(\cdot | x_t)$ for each position i and time t . In addition, we are
141 given N pre-trained scalar objective functions $s_n : \mathcal{S} \rightarrow \mathbb{R}$, where $n = 1, \dots, N$, and $\tilde{s}_n(x)$ are their
142 normalized counterparts with outputs mapped to $[0, 1]$ to support balanced updates for each objective.
143 The sampling task is to construct a Markov chain whose stationary distribution concentrates on states
144 that approximate the Pareto front of the normalized objectives $\tilde{s}_1, \dots, \tilde{s}_N$.
145

146 3.2 ANNEALED MULTI-OBJECTIVE GUIDANCE
147

148 To direct sampling toward the Pareto front, AReUREDi introduces a scalarized reward
149

$$S_\omega(x) = \min_{1 \leq n \leq N} \omega_n \tilde{s}_n(x),$$

150 where the weight vector $\omega = [\omega_1, \dots, \omega_N]$ lies in the probability simplex Δ^{N-1} and balances the
151 different objectives. This Tchebycheff scalarization promotes solutions that are simultaneously strong
152 across all objectives rather than excelling in only a subset (Miettinen, 1999). The scalarized reward is
153 converted into a guidance weight

$$154 \quad W_{\eta_t, \omega}(x) = \exp(\eta_t S_\omega(x)),$$

155 where the parameter $\eta_t > 0$ controls the strength of the guidance at each iteration t . AReUREDi
156 incorporates an annealing schedule for η_t :

$$157 \quad \eta_t = \eta_{\min} + (\eta_{\max} - \eta_{\min}) \frac{t}{T-1},$$

159 so that the chain begins with a small value of η_t to encourage wide exploration of the state space and
160 gradually increases η_t to focus sampling on high-quality Pareto candidates. This annealing strategy
161 mirrors simulated annealing but operates directly on the scalarized objectives within the discrete flow
framework.

162 3.3 LOCALLY BALANCED PROPOSALS
163

164 Given the current state x_t , AReUReDi updates one coordinate $i \in \{1, \dots, L\}$ at a time using a
165 locally balanced proposal that blends the generative prior of ReDi with the multi-objective guidance.
166 First, a candidate set of replacement tokens is drawn from the ReDi marginal $p_t^i(\cdot | x_t)$, optionally
167 pruned using top-p to retain only the most promising alternatives for computational efficiency. For
168 each candidate token y , the algorithm computes the ratio

$$169 \quad r_i(y; x_t) = \frac{W_{\eta_t, \omega}(x_t^{(i \leftarrow y)})}{W_{\eta_t, \omega}(x_t)}, \\ 170 \\ 171$$

172 which measures the change in scalarized reward if x_t^i were replaced by y . The ratio $r_i(y; x_t)$ is
173 then transformed by a balancing function $g : \mathbb{R}_+ \rightarrow \mathbb{R}_+$ that satisfies the symmetry condition
174 $g(u) = u g(1/u)$. Typical choices include Barker's function $g(u) = \frac{u}{1+u}$ and the square-root
175 function $g(u) = \sqrt{u}$. This symmetry ensures that the resulting Markov chain admits the desired
176 stationary distribution. Using the balanced function, the unnormalized proposal for a candidate token
177 y takes the form

$$178 \quad \tilde{q}_i(y | x_t) = p_t^i(y | x_t) g(r_i(y; x_t)),$$

179 which is then normalized over the candidate set to yield the final proposal distribution $q_i(y | x_t)$.
180 This construction allows the proposal to favor states with higher scalarized reward while remaining
181 reversible with respect to the target distribution.

182 3.4 METROPOLIS-HASTINGS UPDATE
183

184 A candidate token y^* is drawn from the final proposal distribution $q_i(\cdot | x_t)$ and forms the proposed
185 state $x_{\text{prop}} = x_t^{(i \leftarrow y^*)}$. The proposal is accepted with the standard Metropolis-Hastings probability
186 (Hastings, 1970)

$$187 \quad \alpha_i(x_t, x_{\text{prop}}) = \min \left\{ 1, \frac{\pi_{\eta_t, \omega}(x_{\text{prop}}) q_i(x_t^i | x_{\text{prop}})}{\pi_{\eta_t, \omega}(x_t) q_i(y^* | x_t)} \right\}, \\ 188 \\ 189$$

190 where we define $\pi_{\eta_t, \omega}(x) \propto p_1(x) W_{\eta_t, \omega}(x) = p_1(x) \exp(\eta_t S_{\omega}(x))$. With Barker's balancing
191 function, the acceptance probability simplifies to one, ensuring automatic acceptance of proposals
192 and faster mixing. Other choices, such as the square-root function, trade higher acceptance rates for
193 more conservative moves.

194 The annealed, locally balanced updates are repeated for T iterations and end with the final sample
195 x_1 whose objective scores are jointly optimized. Building on the ReDi model's well-calibrated base
196 distribution with low inter-dimensional correlation, AReUReDi safely biases this base toward Pareto-
197 optimal regions while preserving full coverage of the state space, thereby guaranteeing convergence
198 to Pareto-optimal solutions with complete coverage of the Pareto front.

199

200 4 EXPERIMENTS
201

202 To the best of our knowledge, no public datasets exist for benchmarking multi-objective optimization
203 algorithms on biological sequences. We therefore developed two benchmarks to evaluate AReUReDi,
204 focusing on the generation of wild-type peptide sequences and chemically-modified peptide SMILES.
205 These tasks are supported by two core components: the generative models described in Appendix B
206 and the objective-scoring models validated in Appendix E. Leveraging these models, we demonstrate
207 AReUReDi's efficacy on a wide range of tasks and examples.

208 Although AReUReDi provides theoretical guarantees of Pareto optimality and full coverage, in
209 practice, these guarantees hold only in the limit of an infinitely long Markov chain. Reaching
210 the Pareto front with high probability can therefore require a vast number of sampling steps. To
211 improve sampling efficiency in all reported experiments, we introduce a monotonicity constraint that
212 accepts only token updates that increase the weighted sum of the current objective scores. Empirical
213 results prove the accelerated convergence toward high-quality Pareto solutions without altering the
214 underlying optimization objectives (Table 6). Therefore, this monotonicity constraint was involved in
215 all the following experiments.

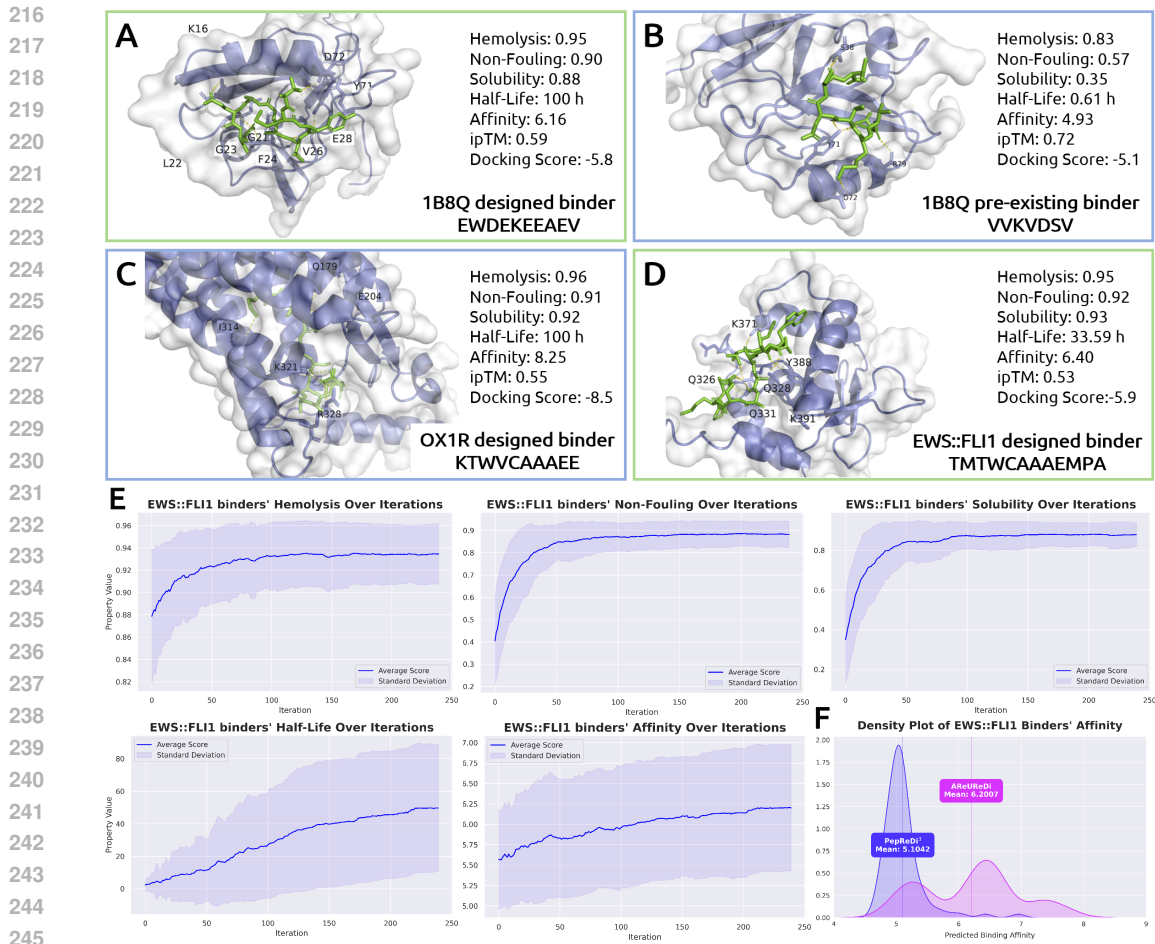


Figure 1: (A), (B) Complex structures of PDB 1B8Q with an AReURedI-designed binder and its pre-existing binder. (C), (D) Complex structures of OX1R and EWS::FLI1 with an AReURedI-designed binder. Five property scores are shown for each binder, along with the ipTM score from AlphaFold3 and docking score from AutoDock VINA. Interacting residues on the target are visualized. (E) Plots showing the mean scores for each property across the number of iterations during AReURedI’s design of binders of length 12-aa for EWS::FLI1. (F) A density plot illustrating the distribution of predicted property scores for AReURedI-designed EWS::FLI1 binders of length 12-aa, compared to the peptides generated unconditionally by PepReDi³.

4.1 AREUREDI EFFECTIVELY BALANCES EACH OBJECTIVE TRADE-OFF

With pre-trained PepReDi in hand, we first focus on validating AReURedI’s capability of balancing multiple conflicting objectives. We performed two sets of experiments for wild-type peptide binder generation with three property guidance, and in ablation experiment settings, we removed one or more objectives. In the binder design task for target 7LUL (hemolysis, solubility, affinity guidance; Table 7), omitting any single guidance causes a collapse in that property, while the remaining guided metrics may modestly improve. Likewise, in the binder design task for target CLK1 (affinity, non-fouling, half-life guidance; Table 8), disabling non-fouling guidance allows half-life to exceed 96 hours but drives non-fouling near zero, and disabling half-life guidance preserves non-fouling yet reduces half-life below 2 hours. In contrast, enabling all guidance signals produces the most balanced profiles across all objectives. These results confirm that AReURedI precisely targets chosen objectives while preserving the flexibility to navigate conflicting objectives and push samples toward the Pareto front.

4.2 AREUREDI GENERATES WILD-TYPE PEPTIDE BINDERS UNDER FIVE PROPERTY GUIDANCE

We next benchmark AReURedI on a wild-type peptide binder generation task guided by five different properties that are critical for therapeutic discovery: hemolysis, non-fouling, solubility, half-life,

270 Table 1: AReUReDi generates wild-type peptide binders for 8 diverse protein targets, optimizing five therapeutic
 271 properties: hemolysis, non-fouling, solubility, half-life (in hours), and binding affinity. Each value represents the
 272 average of 100 AReUReDi-designed binders.

Name	Binder Length	Hemolysis	Non-Fouling	Solubility	Half-Life (h)	Affinity
AMHR2	8	0.9156	0.8613	0.8564	45.73	7.0608
AMHR2	12	0.9384	0.8872	0.8810	52.52	7.2284
AMHR2	16	0.9420	0.8914	0.8755	63.34	7.2533
EWS::FLI1	8	0.9186	0.8630	0.8619	44.77	5.8424
EWS::FLI1	12	0.9345	0.8819	0.8796	59.11	6.2007
EWS::FLI1	16	0.9416	0.8875	0.8807	64.32	6.4195
MYC	8	0.9180	0.8627	0.8627	44.13	6.4082
OX1R	10	0.9302	0.8687	0.8563	50.14	7.1882
DUSP12	9	0.9240	0.8669	0.8633	48.14	6.1276
1B8Q	8	0.9214	0.8680	0.8654	42.63	5.7130
5AZ8	11	0.9293	0.8732	0.8605	58.33	6.2792
7JVS	11	0.9313	0.8840	0.8743	56.49	6.8449

289 and binding affinity. To evaluate AReUReDi in a controlled setting, we designed 100 peptide
 290 binders per target for 8 diverse proteins, structured targets with known binders (3IDJ, 5AZ8, 7JVS),
 291 structured targets without known binders (AMHR2, OX1R, DUSP12), and intrinsically disordered
 292 targets (EWS::FLI1, MYC) (Table 1). Across all targets and across multiple binder lengths, the
 293 generated peptides achieve superior hemolysis rates (0.91-0.94), high non-fouling (>0.86) and
 294 solubility (>0.85), extended half-life (42-64 h), and strong affinity scores (5.7-7.3), demonstrating
 295 both balanced optimization and robustness to sequence length.

296 For the target proteins with pre-existing binders, we compared the property values between their
 297 known binders with AReUReDi-designed ones (Figure 1A,B, A1). The designed binders significantly
 298 outperform the pre-existing binders across all properties without compromising the binding potential,
 299 which is further confirmed by the ipTM scores computed by AlphaFold3 (Abramson et al., 2024)
 300 and docking scores calculated by AutoDock VINA (Trott & Olson, 2010). Although the AReUReDi-
 301 designed binders bind to similar target positions as the pre-existing ones, they differ significantly in
 302 sequence and structure, demonstrating AReUReDi’s capacity to explore the vast sequence space for
 303 optimal designs. For target proteins without known binders, complex structures were visualized using
 304 one of the AReUReDi-designed binders (Figure A2). The corresponding property scores, as well as
 305 ipTM and docking scores, are also displayed. Some of the designed binders showed longer half-life,
 306 while others excelled in non-fouling and solubility, underscoring the comprehensive exploration of
 307 the sequence space by AReUReDi.

308 To evaluate our guided generation strategy, we tracked the mean and standard deviation of five
 309 property scores across 100 generated binders (length 12) targeting EWS::FLI1 at each iteration
 310 (Figure 1E). All five properties steadily improved, with average scores for solubility and non-fouling
 311 properties increasing markedly from 0.4 to 0.9. The large standard deviation observed in the final
 312 half-life and binding affinity values reflects this property’s high sensitivity to guidance, as AReUReDi
 313 balances the trade-offs between multiple conflicting objectives. We further visualized AReUReDi’s
 314 impact by comparing the property distribution of the 100 guided peptides to that of 100 peptides
 315 unconditionally sampled from PepReDi³. The results show that AReUReDi effectively shifted the
 316 distribution towards peptides with higher binding affinity. Collectively, these findings demonstrate
 317 AReUReDi’s capability to steer generation toward simultaneous multi-property optimization.

318 We benchmarked AReUReDi against four established multi-objective optimization (MOO) baselines
 319 (NSGA-III (Deb & Jain, 2013), SMS-EMOA (Beume et al., 2007), SPEA2 (Zitzler et al., 2001),
 320 and MOPSO (Coello & Lechuga, 2002)) on two protein targets: 1B8Q, a small protein with known
 321 peptide binders (Zhang et al., 1999), and PPP5, a larger protein without characterized binders
 322 (Yang et al., 2004) (Table 2). Each method generated 100 candidate binders optimized for five
 323 properties: hemolysis, non-fouling, solubility, half-life, and binding affinity. While AReUReDi
 required longer runtimes than evolutionary baselines, it consistently produced the best trade-offs. For
 both targets, it designed targets with top hemolysis scores, increased non-fouling and solubility by

324
 325 Table 2: AReUREDi outperforms traditional multi-objective optimization algorithms in designing wild-type
 326 peptide binders guided by five objectives. Each value represents the average of 100 designed binders. The table
 327 also records the average runtime for each algorithm to design a single binder. The best result for each metric is
 328 highlighted in bold.

Target	Method	Time (s)	Hemolysis	Non-Fouling	Solubility	Half-Life (h)	Affinity
1B8Q	MOPSO	8.54	0.8934	0.4763	0.4684	4.45	6.0594
	NSGA-III	33.13	0.9138	0.5715	0.5825	7.32	7.2178
	SMS-EMOA	8.21	0.8804	0.3450	0.3511	3.02	5.955
	SPEA2	17.48	0.9181	0.4973	0.5057	4.13	7.3240
	PepTune + DPLM	2.46	0.8547	0.3085	0.3213	1.17	5.2398
	AReUREDi	55	0.9214	0.8680	0.8654	22.93	5.7130
PPP5	MOPSO	11.34	0.9117	0.4711	0.4255	1.77	6.6958
	NSGA-III	37.30	0.9521	0.7138	0.7066	2.90	7.3789
	SMS-EMOA	8.43	0.8758	0.4269	0.4334	1.03	6.2854
	SPEA2	19.02	0.9445	0.6221	0.6098	2.61	7.6253
	PepTune + DPLM	4.80	0.8816	0.2752	0.2636	1.27	5.8454
	AReUREDi	195	0.9412	0.896	0.8832	38.28	6.7186

343
 344 30-50%, maintained competitive binding affinity, and even extended the half-life by a factor of 3-13
 345 relative to the next-best method. These results underscore AReUREDi’s effectiveness in navigating
 346 high-dimensional property landscapes to yield peptide binders with balanced, optimized profiles.
 347

348 We also compared against PepTune (Tang et al., 2025b), a recent masked discrete diffusion model
 349 for peptide design that couples generation with Monte Carlo Tree Search for MOO. PepTune’s
 350 backbone was adapted to the existing DPLM model (Wang et al., 2024) for wild-type peptide
 351 sequence generation. Despite longer runtimes, AReUREDi substantially outperformed PepTune
 352 across all objectives, yielding nearly threefold improvements in non-fouling and solubility and a
 353 22-fold increase in half-life. Together, these comparisons demonstrate that AReUREDi surpasses not
 354 only traditional MOO algorithms but also the current state-of-the-art diffusion-based approach for
 355 multi-objective-guided wild-type peptide binder design.

356 Since AReUREDi requires more computation than PepTune to design the same number of binders, we
 357 compare both methods under a matched wall-clock budget (Table 11). Specifically, the time PepTune
 358 needs to generate 100 binders approximately matches the time AReUREDi needs to generate four 8-
 359 mer binders for 1B8Q and three 16-mer binders for PPP5. For both tasks, the top-2 AReUREDi binders
 360 achieve substantially higher non-fouling, solubility, and half-life, while maintaining comparable
 361 hemolysis and affinity. This comparison shows that AReUREDi produces better multi-objective
 362 trade-offs, even when PepTune is allowed a much larger candidate pool under the same time budget.
 363

364 4.3 AREUREDI GENERATES THERAPEUTIC PEPTIDE SMILES UNDER FOUR PROPERTY 365 GUIDANCE

366 To demonstrate the broad applicability of AReUREDi for multi-objective guided generation of
 367 biological sequences, we employed the rectified SMILESReDi model to design chemically-modified
 368 peptide binder SMILES sequences for five diverse therapeutic targets. These included the metabolic
 369 hormone receptor Glucagon-like peptide-1 receptor (GLP1), the iron transport protein Transferrin
 370 receptor (TfR), the Neural Cell Adhesion Molecule 1 (NCAM1), the neurotransmitter transporter
 371 GLAST, and the developmental Anti-Müllerian Hormone Receptor Type 2 (AMHR2). For each
 372 target, sequence generation was jointly conditioned on a predicted binding-affinity score to the target
 373 protein, as long as hemolysis, solubility, and non-fouling, to ensure both potency and desirable
 374 physicochemical profiles. Although PepTune is also able to perform multi-property guided design
 375 of peptide-binder SMILES sequences, it does not report average property scores for its generated
 376 binders, making a direct quantitative comparison with AReUREDi infeasible (Tang et al., 2025b).

377 We selected and visualized representative binders with the highest predicted binding affinities for
 378 each target (Figure 2A, A3A,C, A4A,C). All selected binders achieved high scores across hemolysis,

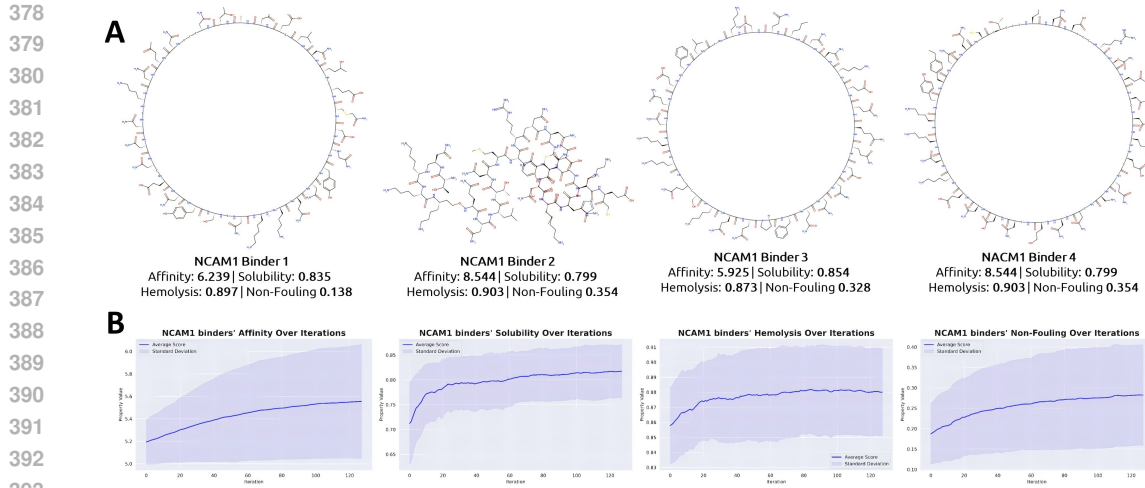


Figure 2: (A) Example 2D SMILES structure of AReUReDi-designed peptide binders with four property scores. (B) Plots showing the mean scores for each property across the number of iterations during AReUReDi’s design of binders of length 200 for NCAM1.

solubility, non-fouling, and binding affinity. During generation, we recorded the mean and standard deviation of all four property scores over 100 binders at each iteration to assess the effectiveness of the multi-objective guidance (Figure 2B, A3B,D, A4B,D). Across all targets, binding affinity scores and non-fouling scores showed steady upward trends throughout the generation process, while hemolysis and solubility scores fluctuated, indicating AReUReDi’s effort to balance the four conflicting objectives. Moreover, AReUReDi produces valid sequences with substantially higher diversity and lower SNN than PepTune, indicating both superior novelty and structural variability (Table 5). These findings highlight the versatility and reliability of AReUReDi for the *de novo* design of chemically modified peptide binders across a wide range of therapeutic targets.

4.4 ABLATION STUDIES FOR RECTIFICATION AND ANNEALED GUIDANCE STRENGTH

To determine if rectification offers an advantage over standard discrete flow matching, we compared the performance of AReUReDi using three generative models: the base PepReDi model (no rectification), PepReDi (three rounds of rectification), and PepDFM, a standard discrete flow model that follows Gat et al. (2024) and was trained on the same data (Appendix C.3). Under the three settings, wild-type binders were designed for two distinct protein targets: 5AZ8 and AMHR2 (Table 9). For the AMHR2 target, the rectified model achieved the highest scores across all five properties, with its predicted half-life surpassing the next-best method by nearly 13 hours. For the 5AZ8 target, the rectified model yielded a significantly higher half-life while maintaining comparable performance on other metrics. These results indicate that by lowering conditional TC and improving the quality of the probability path, rectification enables AReUReDi to achieve stronger Pareto trade-offs on the more demanding objectives.

We further demonstrated the advantage of using an annealed guidance strength (Table 10). AReUReDi was applied to design wild-type peptide binders for two distinct proteins: a structured protein with known binders (PDB 1DDV) and an intrinsically disordered protein without known binders (P53). Across both targets, any fixed guidance strength, whether set to η_{\min} , η_{\max} , or their midpoint, failed to match the performance achieved with an annealed schedule. For 1DDV, annealing produced binders with markedly higher half-life and the best solubility, while maintaining hemolysis, non-fouling, and affinity scores that meet or exceed those of all fixed- η settings. A similar trend holds for P53, where the annealing schedule consistently delivers the strongest results across all objectives. These findings confirm that gradually increasing the guidance strength enables AReUReDi to attain more favorable Pareto trade-offs, enhancing challenging properties such as half-life without sacrificing other therapeutic metrics.

432 5 RELATED WORKS

434 **Online Multi-Objective Optimization.** Recent work in multi-objective guided generation has
 435 focused on online or sequential decision-making, where solutions are refined with new data (Gruver
 436 et al., 2023; Jain et al., 2023; Stanton et al., 2022; Ahmadianshalchi et al., 2024). A common
 437 approach is Bayesian optimization (BO), which builds a surrogate model and proposes evaluations
 438 via acquisition functions (Yu et al., 2020; Shahriari et al., 2015). Multi-objective BO often uses
 439 advanced criteria such as EHVI (Emmerich & Klinkenberg, 2008), information gain (Belakaria et al.,
 440 2021), or scalarization (Knowles, 2006; Zhang & Li, 2007; Paria et al., 2020). While AReUReDi also
 441 employs Tchebycheff scalarization, it operates in an offline setting, where each sequence requires
 442 costly evaluation. This contrasts with the sequential, feedback-driven nature of online methods,
 443 making direct comparison inappropriate.

444 **Tchebycheff Scalarization.** Tchebycheff scalarization can identify any Pareto-optimal point and
 445 is widely used in multi-objective optimization (Miettinen, 1999). Recent variants include smooth
 446 scalarization for gradient-based algorithms (Lin et al., 2024b) and OMD-TCH for online learning (Liu
 447 et al., 2024). AReUReDi is, to our knowledge, the first to apply Tchebycheff scalarization for offline
 448 generative design of discrete therapeutic sequences. Future work may extend to many-objective
 449 problems or alternative utility functions (Lin et al., 2024a; Tu et al., 2023).

450 **Diffusion and Flow Matching.** Generative approaches such as ParetoFlow and PGD-MOO adapt
 451 flow matching or diffusion models for multi-objective optimization (Yuan et al., 2024; Annadani et al.,
 452 2025). These operate in continuous or latent spaces, whereas AReUReDi is designed for discrete
 453 token spaces inherent to biological sequences. This domain mismatch precludes direct benchmarking.

454 **Biomolecule Generation.** Offline multi-objective frameworks such as EGD and MUDM have
 455 optimized molecules with multiple properties (Sun et al., 2025; Han et al., 2023), but these emphasize
 456 3D structural representations. By contrast, AReUReDi is sequence-only, operating directly over
 457 amino acids or SMILES, which makes structural methods unsuitable as direct comparators.

459 6 DISCUSSION

461 In this work, we have presented **AReUReDi**, a multi-objective optimization framework that extends
 462 rectified discrete flows to generate biomolecular sequences satisfying multiple, often conflicting,
 463 properties. By integrating annealed Tchebycheff scalarization, locally balanced proposals, and
 464 Metropolis-Hastings updates, AReUReDi provides theoretical guarantees of convergence to the Pareto
 465 front while maintaining full coverage of the solution space. Built on high-quality base generators
 466 such as PepReDi and SMILESReDi, the method demonstrates broad applicability across amino acid
 467 sequences and chemically modified peptide SMILES. Superior *in silico* results establish AReUReDi
 468 as a general, theoretically-grounded tool for multi-property-guided biomolecular sequence design.

469 While AReUReDi excels in domains like wild-type and chemically-modified peptide designs, future
 470 work will extend to other biological modalities, including DNA, RNA, antibodies, and combinatorial
 471 genotype libraries, where multi-objective trade-offs are central. From a theoretical perspective,
 472 improving AReUReDi’s efficiency while maintaining the Pareto convergence guarantees and incorpo-
 473 rating uncertainty-aware or feedback-driven guidance remain key directions to explore. Ultimately,
 474 AReUReDi provides a foundation for designing the next generation of therapeutic molecules that are
 475 not only potent but also explicitly optimized for the diverse properties required for clinical success.

477 REPRODUCIBILITY STATEMENT

479 We ensure reproducibility through detailed theoretical, algorithmic, and experimental descriptions
 480 of AReUReDi. The complete procedure is formally described in the main text with proofs of
 481 convergence guarantees, including the rectified discrete flow foundation, annealed Tchebycheff
 482 scalarization, locally balanced proposals, and Metropolis-Hastings updates. Architectures, training
 483 details, and datasets for all base generators (PepReDi, SMILESReDi, and PepDFM) are reported
 484 with quantitative metrics in the Results and Appendix. Hyperparameter settings, annealing schedules,
 485 and sensitivity analyses are provided to facilitate replication, and ablation studies are included to
 assess the impact of key design choices. Benchmark comparisons against classical multi-objective

486 optimization baselines and diffusion-based methods are tabulated for reference. All datasets used in
487 this work (PepNN, BioLip2, PPIRef, peptide property datasets, and peptide SMILES collections) are
488 publicly available. We will release code, pretrained checkpoints, and sampling scripts for AReUReDi
489 to enable full reproducibility.
490

491 ETHICS STATEMENT 492

493 This work develops a general generative modeling framework for multi-objective sequence design,
494 with demonstrations on peptide and peptide-SMILES generation. All datasets are publicly available
495 and non-sensitive, consisting of peptide property measurements, protein-peptide interaction sets,
496 and peptide SMILES representations. No human subjects, patient data, or animal experiments were
497 involved. Potential risks include the misuse of generative models for harmful molecule design or
498 the uncontrolled release of potent sequences. To mitigate these risks, we will release code and
499 pretrained models strictly under a research-only license and provide documentation that emphasizes
500 safe and responsible use. The anticipated societal benefits, such as improving therapeutic peptide
501 design, enhancing drug safety profiles, and enabling efficient exploration of biological sequence
502 space, substantially outweigh these potential risks. We encourage future users of AReUReDi to adopt
503 similar safeguards when applying the method to other molecular domains.
504
505
506
507
508
509
510
511
512
513
514
515
516
517
518
519
520
521
522
523
524
525
526
527
528
529
530
531
532
533
534
535
536
537
538
539

540 REFERENCES
541

542 Osama Abdin, Satra Nim, Han Wen, and Philip M Kim. Pepnn: a deep attention model for the
543 identification of peptide binding sites. *Communications biology*, 5(1):503, 2022.

544

545 Josh Abramson, Jonas Adler, Jack Dunger, Richard Evans, Tim Green, Alexander Pritzel, Olaf
546 Ronneberger, Lindsay Willmore, Andrew J Ballard, Joshua Bambbrick, et al. Accurate structure
547 prediction of biomolecular interactions with alphafold 3. *Nature*, pp. 1–3, 2024.

548

549 Alaleh Ahmadianshalchi, Syrine Belakaria, and Janardhan Rao Doppa. Pareto front-diverse batch
550 multi-objective bayesian optimization. In *Proceedings of the AAAI Conference on Artificial
551 Intelligence*, volume 38, pp. 10784–10794, 2024.

552

553 Takuya Akiba, Shotaro Sano, Toshihiko Yanase, Takeru Ohta, and Masanori Koyama. Optuna: A next-
554 generation hyperparameter optimization framework. In *International Conference on Knowledge
555 Discovery and Data Mining*, pp. 2623–2631, 2019.

556

557 Yashas Annadani, Syrine Belakaria, Stefano Ermon, Stefan Bauer, and Barbara E Engel-
558 hardt. Preference-guided diffusion for multi-objective offline optimization. *arXiv preprint
arXiv:2503.17299*, 2025.

559

560 Valentin Artemyev, Anna Gubaeva, Anastasiia Iu Paremskaia, Amina A Dzhioeva, Andrei Deviatkin,
561 Sofya G Feoktistova, Olga Mityaeva, and Pavel Yu Volchkov. Synthetic promoters in gene therapy:
562 Design approaches, features and applications. *Cells*, 13(23):1963, 2024.

563

564 Syrine Belakaria, Aryan Deshwal, and Janardhan Rao Doppa. Output space entropy search framework
565 for multi-objective bayesian optimization. *Journal of artificial intelligence research*, 72:667–715,
566 2021.

567

568 Gleb Beliakov and Kieran F Lim. Challenges of continuous global optimization in molecular structure
569 prediction. *European journal of operational research*, 181(3):1198–1213, 2007.

570

571 Nicola Beume, Boris Naujoks, and Michael Emmerich. Sms-emoa: Multiobjective selection based
572 on dominated hypervolume. *European journal of operational research*, 181(3):1653–1669, 2007.

573

574 Alessandra Bigi, Eva Lombardo, Roberta Cascella, and Cristina Cecchi. The toxicity of protein
575 aggregates: new insights into the mechanisms, 2023.

576

577 Jenny Bostrom, Chingwei V Lee, Lauric Haber, and Germaine Fuh. Improving antibody binding
578 affinity and specificity for therapeutic development. In *Therapeutic Antibodies: Methods and
579 Protocols*, pp. 353–376. Springer, 2008.

580

581 Anton Bushuiev, Roman Bushuiev, Petr Kouba, Anatolii Filkin, Marketa Gabrielova, Michal Gabriel,
582 Jiri Sedlar, Tomas Pluskal, Jiri Damborsky, Stanislav Masurenko, et al. Learning to design
583 protein-protein interactions with enhanced generalization. *arXiv preprint arXiv:2310.18515*, 2023.

584

585 Andrew Campbell, Jason Yim, Regina Barzilay, Tom Rainforth, and Tommi Jaakkola. Generative
586 flows on discrete state-spaces: Enabling multimodal flows with applications to protein co-design. In
587 *Forty-first International Conference on Machine Learning*, 2024. URL <https://openreview.net/forum?id=kQwSbv0BR4>.

588

589 Shengfu Chen, Zhiqiang Cao, and Shaoyi Jiang. Ultra-low fouling peptide surfaces derived from
590 natural amino acids. *Biomaterials*, 30(29):5892–5896, 2009.

591

592 CA Coello Coello and Maximino Salazar Lechuga. Mopso: A proposal for multiple objective particle
593 swarm optimization. In *Proceedings of the 2002 Congress on Evolutionary Computation. CEC'02
(Cat. No. 02TH8600)*, volume 2, pp. 1051–1056. IEEE, 2002.

594

595 Oscar Davis, Samuel Kessler, Mircea Petrache, Ismail Ceylan, Michael Bronstein, and Joey Bose.
596 Fisher flow matching for generative modeling over discrete data. *Advances in Neural Information
597 Processing Systems*, 37:139054–139084, 2024.

594 Kalyanmoy Deb. Multi-objective optimisation using evolutionary algorithms: an introduction.
 595 In *Multi-objective evolutionary optimisation for product design and manufacturing*, pp. 3–34.
 596 Springer, 2011.

597 Kalyanmoy Deb and Himanshu Jain. An evolutionary many-objective optimization algorithm
 598 using reference-point-based nondominated sorting approach, part i: solving problems with box
 599 constraints. *IEEE transactions on evolutionary computation*, 18(4):577–601, 2013.

600 Ian Dunn and David Ryan Koes. Exploring discrete flow matching for 3d de novo molecule generation.
 601 *ArXiv*, pp. arXiv–2411, 2024.

602 Vera D’Aloisio, Paolo Dognini, Gillian A Hutcheon, and Christopher R Coxon. Peptherdia: database
 603 and structural composition analysis of approved peptide therapeutics and diagnostics. *Drug
 604 Discovery Today*, 26(6):1409–1419, 2021.

605 Michael Emmerich and Jan-willem Klinkenberg. The computation of the expected improvement in
 606 dominated hypervolume of pareto front approximations. *Rapport technique, Leiden University*, 34:
 607 7–3, 2008.

608 Keld Fosgerau and Torsten Hoffmann. Peptide therapeutics: current status and future directions.
 609 *Drug discovery today*, 20(1):122–128, 2015.

610 Trevor S Frisby and Christopher James Langmead. Bayesian optimization with evolutionary and
 611 structure-based regularization for directed protein evolution. *Algorithms for Molecular Biology*, 16
 612 (1):13, 2021.

613 Itai Gat, Tal Remez, Neta Shaul, Felix Kreuk, Ricky TQ Chen, Gabriel Synnaeve, Yossi Adi, and
 614 Yaron Lipman. Discrete flow matching. *Advances in Neural Information Processing Systems*, 37:
 615 133345–133385, 2024.

616 Nate Gruver, Samuel Stanton, Nathan Frey, Tim GJ Rudner, Isidro Hotzel, Julien Lafrance-Vanasse,
 617 Arvind Rajpal, Kyunghyun Cho, and Andrew G Wilson. Protein design with guided discrete
 618 diffusion. *Advances in neural information processing systems*, 36:12489–12517, 2023.

619 Chakradhar Guntuboina, Adrita Das, Parisa Mollaei, Seongwon Kim, and Amir Barati Farimani.
 620 Peptidebert: A language model based on transformers for peptide property prediction. *The Journal
 621 of Physical Chemistry Letters*, 14(46):10427–10434, 2023.

622 Xu Han, Caihua Shan, Yifei Shen, Can Xu, Han Yang, Xiang Li, and Dongsheng Li. Training-
 623 free multi-objective diffusion model for 3d molecule generation. In *The Twelfth International
 624 Conference on Learning Representations*, 2023.

625 W Keith Hastings. Monte carlo sampling methods using markov chains and their applications. 1970.

626 Moksh Jain, Sharath Chandra Raparthy, Alex Hernández-García, Jarrid Rector-Brooks, Yoshua
 627 Bengio, Santiago Miret, and Emmanuel Bengio. Multi-objective gflownets. In *International
 628 conference on machine learning*, pp. 14631–14653. PMLR, 2023.

629 Shipra Jain, Srijanee Gupta, Sumeet Patiyal, and Gajendra PS Raghava. Thpdb2: compilation of fda
 630 approved therapeutic peptides and proteins. *Drug Discovery Today*, pp. 104047, 2024.

631 Joshua Knowles. Parego: A hybrid algorithm with on-line landscape approximation for expensive
 632 multiobjective optimization problems. *IEEE transactions on evolutionary computation*, 10(1):
 633 50–66, 2006.

634 Evan Komp, Christian Phillips, Lauren M Lee, Shayna M Fallin, Humood N Alanzi, Marlo Zorman,
 635 Michelle E McCully, and David AC Beck. Neural network conditioned to produce thermophilic
 636 protein sequences can increase thermal stability. *Scientific Reports*, 15(1):14124, 2025.

637 Ryan P Kreiser, Aidan K Wright, Natalie R Block, Jared E Hollows, Lam T Nguyen, Kathleen
 638 LeForte, Benedetta Mannini, Michele Vendruscolo, and Ryan Limbocker. Therapeutic strategies
 639 to reduce the toxicity of misfolded protein oligomers. *International journal of molecular sciences*,
 640 21(22):8651, 2020.

648 Yibo Li, Liangren Zhang, and Zhenming Liu. Multi-objective de novo drug design with conditional
 649 graph generative model. *Journal of cheminformatics*, 10:1–24, 2018.
 650

651 Xi Lin, Yilu Liu, Xiaoyuan Zhang, Fei Liu, Zhenkun Wang, and Qingfu Zhang. Few for many:
 652 Tchebycheff set scalarization for many-objective optimization. *arXiv preprint arXiv:2405.19650*,
 653 2024a.

654 Xi Lin, Xiaoyuan Zhang, Zhiyuan Yang, Fei Liu, Zhenkun Wang, and Qingfu Zhang. Smooth
 655 tchebycheff scalarization for multi-objective optimization. *arXiv preprint arXiv:2402.19078*,
 656 2024b.

657 Zeming Lin, Halil Akin, Roshan Rao, Brian Hie, Zhongkai Zhu, Wenting Lu, Nikita Smetanin,
 658 Robert Verkuil, Ori Kabeli, Yaniv Shmueli, et al. Evolutionary-scale prediction of atomic-level
 659 protein structure with a language model. *Science*, 379(6637):1123–1130, 2023.

660 Meitong Liu, Xiaoyuan Zhang, Chulin Xie, Kate Donahue, and Han Zhao. Online mirror descent for
 661 tchebycheff scalarization in multi-objective optimization. *arXiv preprint arXiv:2410.21764*, 2024.

662 Xingchao Liu, Chengyue Gong, and qiang liu. Flow straight and fast: Learning to generate and transfer
 663 data with rectified flow. In *The Eleventh International Conference on Learning Representations*,
 664 2023. URL <https://openreview.net/forum?id=XVjTT1nw5z>.

665 Deepika Mathur, Satya Prakash, Priya Anand, Harpreet Kaur, Piyush Agrawal, Ayesha Mehta, Rajesh
 666 Kumar, Sandeep Singh, and Gajendra PS Raghava. Peplife: a repository of the half-life of peptides.
 667 *Scientific reports*, 6(1):36617, 2016.

668 Richard Michael, Simon Bartels, Miguel González-Duque, Yevgen Zainchkovskyy, Jes Frellsen,
 669 Søren Hauberg, and Wouter Boomsma. A continuous relaxation for discrete bayesian optimization.
 670 *arXiv preprint arXiv:2404.17452*, 2024.

671 K. Miettinen. *Nonlinear multiobjective optimization*. Kluwer, Boston, USA, 1999.

672 Stephanie E Mohr, Yanhui Hu, Benjamin Ewen-Campen, Benjamin E Housden, Raghuvir Viswanatha,
 673 and Norbert Perrimon. Crispr guide rna design for research applications. *The FEBS journal*, 283
 674 (17):3232–3238, 2016.

675 Gita Naseri and Mattheos AG Koffas. Application of combinatorial optimization strategies in
 676 synthetic biology. *Nature communications*, 11(1):2446, 2020.

677 Atef Nehdi, Nosaibah Samman, Vanessa Aguilar-Sánchez, Azer Farah, Emre Yurdusev, Mohamed
 678 Boudjelal, and Jonathan Perreault. Novel strategies to optimize the amplification of single-stranded
 679 dna. *Frontiers in Bioengineering and Biotechnology*, 8:401, 2020.

680 Hunter Nisonoff, Junhao Xiong, Stephan Allenspach, and Jennifer Listgarten. Unlocking guidance for
 681 discrete state-space diffusion and flow models. *Proceedings of the 13th International Conference
 682 on Learning Representations (ICLR)*, 2025.

683 Biswajit Paria, Kirthevasan Kandasamy, and Barnabás Póczos. A flexible framework for multi-
 684 objective bayesian optimization using random scalarizations. In *Uncertainty in Artificial Intelli-
 685 gence*, pp. 766–776. PMLR, 2020.

686 Fabian Pedregosa, Gaël Varoquaux, Alexandre Gramfort, Vincent Michel, Bertrand Thirion, Olivier
 687 Grisel, Mathieu Blondel, Peter Prettenhofer, Ron Weiss, Vincent Dubourg, Jake Vanderplas,
 688 Alexandre Passos, David Cournapeau, Matthieu Brucher, Matthieu Perrot, and Édouard Duchesnay.
 689 Scikit-learn: Machine learning in python. *J. Mach. Learn. Res.*, 12(null):2825–2830, November
 690 2011. ISSN 1532-4435.

691 William Peebles and Saining Xie. Scalable diffusion models with transformers. *arXiv preprint
 692 arXiv:2212.09748*, 2022.

693 M Pirtskhalava, B Vishnepolsky, and M Grigolava. Transmembrane and antimicrobial peptides.
 694 hydrophobicity, amphiphilicity and propensity to aggregation. *arXiv preprint arXiv:1307.6160*,
 695 2013.

702 Dillon J Rinauro, Fabrizio Chiti, Michele Vendruscolo, and Ryan Limbocker. Misfolded protein
 703 oligomers: Mechanisms of formation, cytotoxic effects, and pharmacological approaches against
 704 protein misfolding diseases. *Molecular Neurodegeneration*, 19(1):20, 2024.

705

706 Olaf Ronneberger, Philipp Fischer, and Thomas Brox. U-net: Convolutional networks for biomedical
 707 image segmentation. In *Medical image computing and computer-assisted intervention—MICCAI
 708 2015: 18th international conference, Munich, Germany, October 5-9, 2015, proceedings, part III
 709 18*, pp. 234–241. Springer, 2015.

710

711 Subham Sekhar Sahoo, Marianne Arriola, Yair Schiff, Aaron Gokaslan, Edgar Marroquin, Justin T
 712 Chiu, Alexander Rush, and Volodymyr Kuleshov. Simple and effective masked diffusion language
 713 models. *Advances in Neural Information Processing Systems*, 2024.

714

715 Henri Schmidt, Minsi Zhang, Dimitar Chakarov, Vineet Bansal, Haralambos Mourelatos, Francisco J
 716 Sánchez-Rivera, Scott W Lowe, Andrea Ventura, Christina S Leslie, and Yuri Pritykin. Genome-
 717 wide crispr guide rna design and specificity analysis with guidescan2. *Genome biology*, 26(1):
 718 1–25, 2025.

719

720 Bobak Shahriari, Kevin Swersky, Ziyu Wang, Ryan P Adams, and Nando De Freitas. Taking the
 721 human out of the loop: A review of bayesian optimization. *Proceedings of the IEEE*, 104(1):
 722 148–175, 2015.

723

724 Neelam Sharma, Leimarembi Devi Naorem, Shipra Jain, and Gajendra PS Raghava. Toxinpred2: an
 725 improved method for predicting toxicity of proteins. *Briefings in bioinformatics*, 23(5):bbac174,
 726 2022.

727

728 Tiago Sousa, João Correia, Vitor Pereira, and Miguel Rocha. Combining multi-objective evolutionary
 729 algorithms with deep generative models towards focused molecular design. In *Applications of
 730 Evolutionary Computation: 24th International Conference, EvoApplications 2021, Held as Part of
 731 EvoStar 2021, Virtual Event, April 7–9, 2021, Proceedings 24*, pp. 81–96. Springer, 2021.

732

733 Samuel Stanton, Wesley Maddox, Nate Gruver, Phillip Maffettone, Emily Delaney, Peyton Greenside,
 734 and Andrew Gordon Wilson. Accelerating bayesian optimization for biological sequence design
 735 with denoising autoencoders. In *International conference on machine learning*, pp. 20459–20478.
 736 PMLR, 2022.

737

738 Hannes Stark, Bowen Jing, Chenyu Wang, Gabriele Corso, Bonnie Berger, Regina Barzilay, and
 739 Tommi Jaakkola. Dirichlet flow matching with applications to dna sequence design. *Proceedings
 740 of the 41st International Conference on Machine Learning (ICML)*, 2024.

741

742 Jianlin Su, Murtadha Ahmed, Yu Lu, Shengfeng Pan, Wen Bo, and Yunfeng Liu. Roformer: Enhanced
 743 transformer with rotary position embedding. *Neurocomputing*, 568:127063, 2024.

744

745 Ruiqing Sun, Dawei Feng, Sen Yang, Yijie Wang, and Huaimin Wang. Evolutionary training-
 746 free guidance in diffusion model for 3d multi-objective molecular generation. *arXiv preprint
 747 arXiv:2505.11037*, 2025.

748

749 R Swanson. Long live peptides—evolution of peptide half-life extension technologies and emerging
 750 hybrid approaches. *Drug Discovery World*, 15:57–61, 2014.

751

752 Sophia Tang, Yinuo Zhang, and Pranam Chatterjee. Gumbel-softmax flow matching with straight-
 753 through guidance for controllable biological sequence generation. *arXiv preprint arXiv:2503.17361*,
 2025a.

754

755 Sophia Tang, Yinuo Zhang, and Pranam Chatterjee. Peptune: De novo generation of therapeutic
 756 peptides with multi-objective-guided discrete diffusion. *Proceedings of the 41st International
 757 Conference on Machine Learning (ICML)*, 2025b.

Masahiro Tominaga, Yoko Shima, Kenta Nozaki, Yoichiro Ito, Masataka Someda, Yuji Shoya,
 Noritaka Hashii, Chihiro Obata, Miho Matsumoto-Kitano, Kohei Suematsu, et al. Designing strong
 inducible synthetic promoters in yeasts. *Nature Communications*, 15(1):10653, 2024.

756 Oleg Trott and Arthur J Olson. Autodock vina: improving the speed and accuracy of docking with
 757 a new scoring function, efficient optimization, and multithreading. *Journal of computational*
 758 *chemistry*, 31(2):455–461, 2010.

759

760 Kotaro Tsuboyama, Justas Dauparas, Jonathan Chen, Elodie Laine, Yasser Mohseni Behbahani,
 761 Jonathan J Weinstein, Niall M Mangan, Sergey Ovchinnikov, and Gabriel J Rocklin. Mega-scale
 762 experimental analysis of protein folding stability in biology and design. *Nature*, 620(7973):
 763 434–444, 2023.

764 Ben Tu, Nikolas Kantas, Robert M Lee, and Behrang Shafei. Multi-objective optimisation via the r2
 765 utilities. *arXiv preprint arXiv:2305.11774*, 2023.

766 Tsuyoshi Ueno, Trevor David Rhone, Zhufeng Hou, Teruyasu Mizoguchi, and Koji Tsuda. Combo:
 767 An efficient bayesian optimization library for materials science. *Materials discovery*, 4:18–21,
 768 2016.

769

770 Xinyou Wang, Zaixiang Zheng, Fei Ye, Dongyu Xue, Shujian Huang, and Quanquan Gu. Diffusion
 771 language models are versatile protein learners. *arXiv preprint arXiv:2402.18567*, 2024.

772 Jing Yang, S Mark Roe, Matthew J Cliff, Mark A Williams, John E Ladbury, Patricia T W Cohen, and
 773 David Barford. Molecular basis for tpr domain-mediated regulation of protein phosphatase 5. *The*
 774 *EMBO Journal*, 24(1):1–10, December 2004. ISSN 1460-2075. doi: 10.1038/sj.emboj.7600496.
 775 URL <http://dx.doi.org/10.1038/sj.emboj.7600496>.

776 Yinghua Yao, Yuangang Pan, Jing Li, Ivor Tsang, and Xin Yao. Proud: Pareto-guided diffusion
 777 model for multi-objective generation. *Machine Learning*, 113(9):6511–6538, 2024.

778

779 Jaehoon Yoo, Wonjung Kim, and Seunghoon Hong. Redi: Rectified discrete flow. *arXiv preprint*
 780 *arXiv:2507.15897*, 2025.

781 Tianhe Yu, Saurabh Kumar, Abhishek Gupta, Sergey Levine, Karol Hausman, and Chelsea Finn.
 782 Gradient surgery for multi-task learning. *Advances in neural information processing systems*, 33:
 783 5824–5836, 2020.

784 Ye Yuan, Can Chen, Christopher Pal, and Xue Liu. Paretoflow: Guided flows in multi-objective
 785 optimization. *arXiv preprint arXiv:2412.03718*, 2024.

786

787 Chengxin Zhang, Xi Zhang, Peter L Freddolino, and Yang Zhang. Biolip2: an updated structure
 788 database for biologically relevant ligand–protein interactions. *Nucleic Acids Research*, 52(D1):
 789 D404–D412, 2024.

790

791 Mingjie Zhang, Hidehito Tochio, Qiang Zhang, Pravat Mandal, and Ming Li. Solution structure of
 792 the extended neuronal nitric oxide synthase pdz domain complexed with an associated peptide.
 793 *Nature Structural Biology*, 6(5):417–421, May 1999. ISSN 1072-8368. doi: 10.1038/8216. URL
 794 <http://dx.doi.org/10.1038/8216>.

795

796 Qingfu Zhang and Hui Li. Moea/d: A multiobjective evolutionary algorithm based on decomposition.
 797 *IEEE Transactions on evolutionary computation*, 11(6):712–731, 2007.

798

799 Ruochi Zhang, Haoran Wu, Yuting Xiu, Kewei Li, Ningning Chen, Yu Wang, Yan Wang, Xin
 800 Gao, and Fengfeng Zhou. Pepland: a large-scale pre-trained peptide representation model for
 801 a comprehensive landscape of both canonical and non-canonical amino acids. *arXiv preprint*
 802 *arXiv:2311.04419*, 2023.

803

804 Ruimin Zhou, Zhaoyan Jiang, Chen Yang, Jianwei Yu, Jirui Feng, Muhammad Abdullah Adil, Dan
 805 Deng, Wenjun Zou, Jianqi Zhang, Kun Lu, et al. All-small-molecule organic solar cells with over
 806 14% efficiency by optimizing hierarchical morphologies. *Nature communications*, 10(1):5393,
 807 2019.

808

809 Eckart Zitzler and Lothar Thiele. Multiobjective optimization using evolutionary algorithms—a
 810 comparative case study. In *International conference on parallel problem solving from nature*, pp.
 811 292–301. Springer, 1998.

812

813 Eckart Zitzler, Marco Laumanns, and Lothar Thiele. Spea2: Improving the strength pareto evolution-
 814 ary algorithm. *TIK report*, 103, 2001.

810 **A THEORETICAL GUARANTEES**
811

812 In this section, we establish that AReUReDi converges to Pareto-optimal solutions while preserving
813 coverage of the entire Pareto front. We assume throughout that the state space \mathcal{S} is finite, all objective
814 functions s_n are bounded, and their normalized versions \tilde{s}_n map to $[0, 1]$.
815

816 **A.1 PRELIMINARY DEFINITIONS**
817

818 **Definition (Pareto Optimality).** A state $x^* \in \mathcal{S}$ is *Pareto optimal* if there exists no $y \in \mathcal{S}$ such that
819 $\tilde{s}_n(y) \geq \tilde{s}_n(x^*)$ for all $n \in \{1, \dots, N\}$ with strict inequality for at least one n .
820

821 **Definition (Pareto Front).** The Pareto front is $\mathcal{P} = \{x \in \mathcal{S} : x \text{ is Pareto optimal}\}$.
822

823 **Definition (Interior Weight Vector).** A weight vector $\omega \in \Delta^{N-1}$ is *interior* if $\omega_n > 0$ for all n .
824

825 **A.2 MAIN THEORETICAL RESULTS**
826

827 **Theorem (Invariance).** The Markov kernel defined by the Locally Balanced Proposal (LBP) and
828 Metropolis–Hastings update leaves the distribution
829

830
$$\pi_{\eta, \omega}(x) \propto p_1(x) \exp(\eta S_\omega(x))$$

831 invariant for every guidance strength $\eta > 0$ and weight vector $\omega \in \Delta^{N-1}$.
832

833 *Proof.* We prove this in two steps: first showing that single-coordinate updates preserve detailed
834 balance, then that random-scan mixtures preserve invariance.
835

836 **Step 1: Single-coordinate detailed balance.** Let x and x' differ only at coordinate i , where $x'_i = y$
837 for some token y . The proposal probability is
838

839
$$q_i(y | x) = \frac{p_t^i(y | x_t)g(r_i(y; x_t))}{\sum_{z \in \text{candidates}} p_t^i(z | x_t)g(r_i(z; x_t))},$$

840 where $r_i(y; x_t) = \frac{W_{\eta_t, \omega}(x_t^{(i \leftarrow y)})}{W_{\eta_t, \omega}(x_t)}$ and g satisfies $g(u) = u \cdot g(1/u)$.
841

842 The acceptance probability is
843

844
$$\alpha_i(x, x') = \min \left\{ 1, \frac{\pi_{\eta, \omega}(x')q_i(x_i | x')}{\pi_{\eta, \omega}(x)q_i(y | x)} \right\}.$$

845 By the symmetry property of g and the construction of the proposal, we have
846

847
$$\frac{q_i(y | x)}{q_i(x_i | x')} = \frac{W_{\eta, \omega}(x')}{W_{\eta, \omega}(x)}.$$

848 Since $\pi_{\eta, \omega}(x) = Z^{-1}p_1(x)W_{\eta, \omega}(x)$, it follows that
849

850
$$\frac{\pi_{\eta, \omega}(x')q_i(x_i | x')}{\pi_{\eta, \omega}(x)q_i(y | x)} = 1.$$

851 Therefore, $\alpha_i(x, x') = 1$ and detailed balance is satisfied.
852

853 **Step 2: Random-scan mixture.** The overall kernel is $K(x, x') = \frac{1}{L} \sum_{i=1}^L K_i(x, x')$, where K_i is
854 the kernel for updating coordinate i . Since each K_i satisfies detailed balance with respect to $\pi_{\eta, \omega}$,
855 their convex combination also satisfies detailed balance and hence preserves invariance. \square
856

857 **Theorem (Convergence to Pareto Front).** Fix any $\omega \in \text{int } \Delta^{N-1}$ with strictly positive entries
858 and let $S_\omega(x) = \min_n \omega_n \tilde{s}_n(x)$. If $\eta \rightarrow \infty$, samples drawn from $\pi_{\eta, \omega}(x) \propto p_1(x) \exp(\eta S_\omega(x))$
859 concentrate on the set
860

861
$$\mathcal{F}_\omega = \arg \max_x S_\omega(x),$$

862 and every element of \mathcal{F}_ω is Pareto optimal.
863

864 *Proof. Step 1: Maximizers of S_ω are Pareto optimal.* Suppose $x^* \in \mathcal{F}_\omega$ but x^* is not Pareto
 865 optimal. Then there exists $y \in \mathcal{S}$ with
 866

$$867 \tilde{s}_n(y) \geq \tilde{s}_n(x^*) \forall n, \quad \text{and} \quad \tilde{s}_m(y) > \tilde{s}_m(x^*) \text{ for some } m.$$

868 Since $\omega_n > 0$ for all n , multiplying preserves inequalities. If m is the bottleneck coordinate of
 869 x^* , then $S_\omega(y) > S_\omega(x^*)$, contradiction. Otherwise, equality requires special weight alignments
 870 (measure zero). Thus maximizers are Pareto optimal almost surely.

871 **Step 2: Concentration as $\eta \rightarrow \infty$.** Let $S_\omega^* = \max_x S_\omega(x)$ and $\Delta_\omega = S_\omega^* - \max_{x \notin \mathcal{F}_\omega} S_\omega(x) > 0$.
 872 Then for $x \notin \mathcal{F}_\omega$,

$$873 \pi_{\eta, \omega}(x) \leq e^{-\eta \Delta_\omega} \cdot \frac{p_1(x)}{\sum_{z \in \mathcal{F}_\omega} p_1(z)}.$$

874 Summing gives $\pi_{\eta, \omega}(\mathcal{S} \setminus \mathcal{F}_\omega) \rightarrow 0$ as $\eta \rightarrow \infty$. Hence the mass concentrates on \mathcal{F}_ω . \square
 875

876 **Theorem (Pareto Point Representability).** For every Pareto-optimal state $x^\dagger \in \mathcal{P}$ there exists
 877 $\omega \in \Delta^{N-1}$ such that $x^\dagger \in \arg \max_x S_\omega(x)$. Moreover, if $\tilde{s}_n(x^\dagger) > 0$ for all n , then x^\dagger can be made
 878 the unique maximizer.

879 *Proof.* If $\tilde{s}_n(x^\dagger) > 0$, define

$$880 \omega_n = \frac{1/\tilde{s}_n(x^\dagger)}{\sum_{k=1}^N 1/\tilde{s}_k(x^\dagger)}.$$

881 Then $S_\omega(x^\dagger) = \frac{1}{\sum_k 1/\tilde{s}_k(x^\dagger)}$, and for any $y \neq x^\dagger$, some m satisfies $\tilde{s}_m(y) < \tilde{s}_m(x^\dagger)$, implying
 882 $S_\omega(y) < S_\omega(x^\dagger)$. If some $\tilde{s}_n(x^\dagger) = 0$, perturb objectives by $\varepsilon > 0$ and take the limit. \square
 883

884 **Theorem (Coverage Guarantee).** Let μ be any probability distribution with full support on
 885 $\text{int } \Delta^{N-1}$. If $\omega \sim \mu$ and $\eta \rightarrow \infty$, then the induced sampler visits every Pareto-optimal state
 886 with positive probability.

887 *Proof.* By representability, each Pareto point x^\dagger maximizes S_ω for some interior ω^\dagger . By continuity,
 888 there exists a neighborhood U_{x^\dagger} where x^\dagger remains optimal. Since $\mu(U_{x^\dagger}) > 0$, randomizing ω
 889 ensures x^\dagger is visited with positive probability in the high- η limit. \square
 890

891 **Remark.** The guarantees hold for any finite \mathcal{S} and bounded objectives. In practice, convergence
 892 depends on the chain mixing rate, the annealing schedule for η , and the choice of balancing function
 893 g .

900 B PEPREDI AND SMILESREDI GENERATE DIVERSE AND BIOLOGICALLY 901 PLAUSIBLE SEQUENCES

902 To enable the efficient generation of peptide binders, we developed an unconditional peptide generator,
 903 **PepReDi**, based on the ReDi framework. The model backbone of PepReDi is a Diffusion Transformer
 904 (DiT) architecture (Peebles & Xie, 2022). We trained PepDFM on a custom dataset comprising
 905 approximately 15,000 peptides from the PepNN and BioLip2 datasets, as well as sequences from the
 906 PPIRef dataset, with lengths ranging from 6 to 49 amino acids (Abdin et al., 2022; Zhang et al., 2024;
 907 Bushuiev et al., 2023). Using this trained model, we generated new data couplings containing 10,000
 908 sequences for each peptide length and used them to fine-tune PepReDi in an iterative rectification
 909 procedure. This rectification was performed three times and yielded substantial improvements in
 910 training loss, validation negative log-likelihood (NLL), perplexity (PPL), and conditional TC (Table
 911 4). Notably, the conditional TC rises after the first rectification, likely due to the distributional shift
 912 from the large, model-generated coupling, whose absolute TC can be higher even though ReDi
 913 guarantees a monotonic decrease within each coupling. The low validation NLL and PPL metrics
 914 showcase PepReDi’s reliability to generate biologically plausible wild-type peptide sequences.

915 SMILESReDi adopts the same backbone structure as PepReDi, enhanced with Rotary Positional
 916 Embeddings (RoPE), which effectively captures the relative inter-token interactions in peptide
 917 SMILES (Su et al., 2024). SMILESReDi also incorporates a time-dependent noising schedule to

918 improve its capability to generate valid peptide SMILES sequences (C.2). We applied the same
 919 training data as PepMDLM, a state-of-the-art diffusion model that generates valid peptide SMILES
 920 sequences (Tang et al., 2025b). After only two training epochs, SMILESReDi converged to a
 921 validation NLL of 0.722 and achieved a sampling validity of 76.3% using just 16 generation steps. One
 922 hundred SMILES sequences were then generated by the trained SMILESReDi for each length from 4
 923 to 1035, forming a large and diverse new data coupling. Following a single round of rectification,
 924 the validation NLL further decreased to 0.608, and the sampling validity rose dramatically to 98.6%
 925 with 16 steps and 100% with 32 steps 5. While its similarity-to-nearest-neighbor (SNN) score and
 926 diversity are comparable to those of PepMDLM (details on metrics are provided in Appendix C.2),
 927 SMILESReDi substantially outperforms PepMDLM in validity, highlighting its superior capability of
 928 generating diverse chemically-modified peptide SMILES sequences.
 929

930 C BASE MODEL DETAILS

931 C.1 PEPREDI

932 **Model Architecture.** The backbone of PepReDi is built on a Diffusion Transformer (DiT) framework
 933 implemented within a Masked Diffusion Language Model (MDLM) paradigm (Peebles & Xie, 2022;
 934 Sahoo et al., 2024). Input amino acid sequences are transformed to discrete tokens using the ESM-2-
 935 650M tokenizer (Lin et al., 2023). Tokenized amino acid sequences and time-steps are converted
 936 to continuous embedding vectors using two separate layers, which are then fused and processed
 937 by stacked DiT transformer blocks equipped with multi-head self-attention to capture long-range
 938 dependencies in the amino-acid sequence. Residual connections and layer normalization stabilize the
 939 training dynamics, and a final projection layer outputs token logits for each position.
 940

941 **Dataset Curation.** The dataset for PepReDi training was curated from the PepNN, BioLip2, and
 942 PPIRef dataset (Abdin et al., 2022; Zhang et al., 2024; Bushuiev et al., 2023). All peptides from
 943 PepNN and BioLip2 were included, along with sequences from PPIRef ranging from 6 to 49 amino
 944 acids in length. The dataset was divided into training, validation, and test sets at an 80/10/10 ratio.
 945

946 **Training Strategy.** Training was conducted on a single node equipped with one NVIDIA GPU and
 947 128 GB of GPU memory using the SLURM workload manager. The model was trained for 100
 948 epochs using the Adam optimizer and a learning rate of 1e-4 with weight decay of 1e-5. A learning
 949 rate scheduler with 10 warm-up epochs and cosine decay was used, with initial and minimum learning
 950 rates both 1e-5. The network architecture included a model dimension of 512, 6 transformer layers,
 951 and 8 attention heads, with a vocabulary size of 24 and a maximum sequence length of 100 tokens.
 952 Conditional total correlation estimation was performed using 20 batches and 50 samples per batch to
 953 monitor rectification quality during training. The model checkpoint with the lowest total correlation
 954 was saved. For training rectified models, the same hyperparameter setting was applied, except for the
 955 loaded pre-trained model checkpoint and the weight decay being increased to 2e-5.
 956

957 **Dynamic Batching.** To enhance computational efficiency and manage variable-length token
 958 sequences, we implemented dynamic batching. Drawing inspiration from ESM-2’s approach (Lin et al.,
 959 2023), input peptide sequences were sorted by length to optimize GPU memory utilization, with a
 960 maximum token size of 100 per GPU.
 961

962 **Rectification.** The trained model applied 16 sampling steps to generate 10k sequences for each
 963 peptide length, ranging from 6 to 49, with a temperature hyperparameter set to 1. After generation,
 964 dynamic batching was used to optimize GPU memory utilization for future rectified training.
 965

966 C.2 SMILESREDI

967 **Model Architecture.** SMILESReDi follows the ReDi paradigm and uses a Diffusion Transformer
 968 (DiT) backbone embedded in a Masked Diffusion Language Model (MDLM) design to generate
 969 molecular SMILES sequences (Peebles & Xie, 2022; Sahoo et al., 2024). Input SMILES sequences
 970 are transformed to discrete tokens using the PeptideCLM -23M tokenizer. Tokenized amino acid
 971 sequences and time-steps are converted to continuous embedding vectors using two separate layers.
 972 Both embeddings are then fused and processed by stacked DiT transformer blocks that incorporate
 973 Rotary Positional Embeddings (RoPE) and multi-head attention modules to capture long-range
 974

structural dependencies while preserving positional information (Su et al., 2024). A final layer normalization and linear projection outputs token logits for each position.

Time-dependent bond-aware noising schedule. Peptide SMILES share a conserved backbone of alternating carbonyl and amide groups connected by chemically constrained peptide bonds, while their side chains remain highly diverse. Standard discrete flow matching can corrupt these critical bond tokens too early, hindering the flow from recovering the backbone along the probability path. Inspired by previous work in bond-dependent masking, we devised a time-dependent bond-aware noising schedule that preserves backbone tokens longer than side-chain tokens, allowing the model to reconstruct the invariant scaffold before generating variable side chains. Specifically, for each position j with a bond indicator $b_j \in \{0, 1\}$, the time- t marginal of the probability path is

$$p_t(x_t^{(j)} | x_0^{(j)}, x_1^{(j)}) = [b_j t^\gamma + (1 - b_j)t] \delta_{x_1^{(j)}} + [1 - b_j t^\gamma - (1 - b_j)t] \delta_{x_0^{(j)}}, \quad t \in [0, 1], \gamma > 1,$$

so each token is equal to $x_1^{(j)}$ with the indicated mixture coefficient and to $x_0^{(j)}$ otherwise, ensuring that backbone tokens ($b_j = 1$) transition more slowly than non-bond tokens along the DFM probability path.

Training Strategy. The training is conducted on a 4*A6000 NVIDIA RTX 6000 Ada GPU system with 48 GB of VRAM for 5 epochs. The model checkpoint with the lowest evaluation loss was saved. The Adam optimizer was employed with a learning rate of 1e-4. A learning rate scheduler with 10% total training steps and cosine decay was used, with initial and minimum learning rates both 1e-5. The network architecture included a model dimension of 768, 8 transformer layers, and 8 attention heads. Gradient clip value was set to 1.0 and γ to 2.0 in the time-dependent bond-aware noising schedule. For training rectified models, the same hyperparameter setting was applied, except for the loaded pre-trained model checkpoint and the total training epochs set to 10.

Rectification. The trained model applied 100 sampling steps to generate 100 sequences for each peptide length, ranging from 4 to 1035, with a temperature hyperparameter set to 1. After generation, dynamic batching was used to optimize GPU memory utilization for future rectified training.

Evaluation Metrics.

- **Validity** is defined as the fraction of peptide SMILES that pass the SMILES2PEPTIDE filter (Tang et al., 2025b), indicating that it translates to a synthesizable peptide.
- **Uniqueness** is defined as the fraction of mutually distinct peptide SMILES.
- **Diversity** is defined as one minus the average Tanimoto similarity between the Morgan fingerprints of every pair of generated sequences, which measures the similarity in structure across generated peptides.

$$\text{Diversity} = 1 - \frac{1}{\binom{N_{\text{generated}}}{2}} \sum_{i,j} \frac{\mathbf{f}(\mathbf{x}_i) \cdot \mathbf{f}(\mathbf{x}_j)}{|\mathbf{f}(\mathbf{x}_i)| + |\mathbf{f}(\mathbf{x}_j)| - \mathbf{f}(\mathbf{x}_i) \cdot \mathbf{f}(\mathbf{x}_j)}$$

where $\mathbf{f}(\mathbf{x}_i)$ and $\mathbf{f}(\mathbf{x}_j)$ are the 2048-dimensional Morgan fingerprint with radius 3 for a pair of generated sequences \mathbf{x}_i and \mathbf{x}_j .

- **Similarity to Nearest Neighbor (SNN)** is defined as the maximum Tanimoto similarity between a generated sequence \mathbf{x}_i with a sequence in the dataset $\tilde{\mathbf{x}}_j$.

$$\text{SNN} = \max_{j \in |\mathcal{D}|} \left(\frac{\mathbf{f}(\mathbf{x}_i) \cdot \mathbf{f}(\tilde{\mathbf{x}}_j)}{|\mathbf{f}(\mathbf{x}_i)| + |\mathbf{f}(\tilde{\mathbf{x}}_j)| - \mathbf{f}(\mathbf{x}_i) \cdot \mathbf{f}(\tilde{\mathbf{x}}_j)} \right)$$

C.3 PEPDFM

Model Architecture. The base model is a time-dependent architecture based on U-Net (Ronneberger et al., 2015). It uses two separate embedding layers for sequence and time, followed by five convolutional blocks with varying dilation rates to capture temporal dependencies, while incorporating time-conditioning through dense layers. The final output layer generates logits for each token. We used a polynomial convex schedule with a polynomial exponent of 2.0 for the mixture discrete probability path in the discrete flow matching.

1026 **Dataset Curation.** The dataset for PepDFM training was curated from the PepNN, BioLip2, and
 1027 PPIRef dataset (Abdin et al., 2022; Zhang et al., 2024; Bushuiev et al., 2023). All peptides from
 1028 PepNN and BioLip2 were included, along with sequences from PPIRef ranging from 6 to 49 amino
 1029 acids in length. The dataset was divided into training, validation, and test sets at an 80/10/10 ratio.
 1030

1031 **Training Strategy.** The training is conducted on a 2xH100 NVIDIA NVL GPU system with 94 GB
 1032 of VRAM for 200 epochs with batch size 512. The model checkpoint with the lowest evaluation loss
 1033 was saved. The Adam optimizer was employed with a learning rate 1e-4. A learning rate scheduler
 1034 with 20 warm-up epochs and cosine decay was used, with initial and minimum learning rates both
 1035 1e-5. The embedding dimension and hidden dimension were set to be 512 and 256 respectively for
 1036 the base model.

1037 **Performance.** PepDFM achieved a validation loss of 3.1051. Its low generalized KL loss during
 1038 evaluation demonstrates PepDFM’s strong capability to generate sequences with high biological
 1039 plausibility (Gat et al., 2024).

1040 D OBJECTIVE DESCRIPTION

1041 In this work, five key property objectives are considered in the peptide binder tasks: hemolysis,
 1042 non-fouling, solubility, half-life, and binding affinity. Each of these properties plays a crucial role
 1043 in optimizing the therapeutic potential of peptides. Hemolysis refers to the peptide’s ability to
 1044 minimize red blood cell lysis, ensuring safe systemic circulation (Pirtskhalava et al., 2013). Non-
 1045 fouling properties describe the peptide’s resistance to unwanted interactions with biomolecules, thus
 1046 enhancing its stability and bioavailability in vivo (Chen et al., 2009). Solubility is critical for ensuring
 1047 adequate peptide dissolution in biological fluids, directly influencing its absorption and therapeutic
 1048 efficacy (Fosgerau & Hoffmann, 2015). Half-life indicates the duration for which the peptide remains
 1049 active in circulation, which is vital for reducing dosing frequency (Swanson, 2014). Finally, binding
 1050 affinity measures the strength of the peptide’s interaction with its target, directly correlating to its
 1051 biological activity and potency in therapeutic applications (Bostrom et al., 2008).

1052 E SCORE MODEL DETAILS

1053 We applied the score models from Tang et al. (2025b) to guide the generation of chemically-modified
 1054 peptide binders. We now introduce the score model developed for the wild-type peptide binder
 1055 generation task. We collected hemolysis (9,316), non-fouling (17,185), solubility (18,453), and
 1056 binding affinity (1,781) data for classifier training from the PepLand and PeptideBERT datasets
 1057 (Zhang et al., 2023; Guntuboina et al., 2023). All sequences taken are wild-type L-amino acids and
 1058 are tokenized and represented by the ESM-2 protein language model (Lin et al., 2023).

1059 E.1 BOOSTED TREES FOR CLASSIFICATION

1060 For hemolysis, non-fouling, and solubility classification, we trained XGBoost boosted tree models
 1061 for logistic regression. We split the data into 0.8/0.2 train/validation using stratified splits from
 1062 scikit-learn (Pedregosa et al., 2011) and generated mean-pooled ESM-2-650M (Lin et al., 2023)
 1063 embeddings as input features to the model. We ran 50 trials of OPTUNA (Akiba et al., 2019) search to
 1064 determine the optimal XGBoost hyperparameters (Table 3), tracking the best binary classification F1
 1065 scores. The best models for each property reached F1 scores of 0.58, 0.71, and 0.68 on the validation
 1066 sets respectively.

1067 E.2 BINDING AFFINITY SCORE MODEL

1068 We developed an unpooled reciprocal attention transformer model to predict protein-peptide binding
 1069 affinity, leveraging latent representations from the ESM-2 650M protein language model (Lin
 1070 et al., 2023). Instead of relying on pooled representations, the model retains unpooled token-level
 1071 embeddings from ESM-2, which are passed through convolutional layers followed by cross-attention
 1072 layers. The binding affinity data were split into a 0.8/0.2 ratio, maintaining similar affinity score
 1073 distributions across splits. We used OPTUNA (Akiba et al., 2019) for hyperparameter optimization,
 1074 tracing validation correlation scores. The final model was trained for 50 epochs with a learning rate
 1075 1076 1077 1078 1079

1080

Table 3: XGBoost Hyperparameters for Classification

1081

1082

1083

1084

1085

1086

1087

1088

1089

1090

1091

1092

1093

1094

1095

1096

1097

1098

1099

1100

1101

1102

1103

1104

1105

1106

1107

1108

1109

1110

1111

1112

1113

1114

1115

1116

1117

1118

1119

1120

1121

1122

1123

1124

1125

1126

1127

1128

1129

1130

1131

1132

1133

Hyperparameter	Value/Range
Objective	binary:logistic
Lambda	[1e-8, 10.0]
Alpha	[1e-8, 10.0]
Colsample by Tree	[0.1, 1.0]
Subsample	[0.1, 1.0]
Learning Rate	[0.01, 0.3]
Max Depth	[2, 30]
Min Child Weight	[1, 20]
Tree Method	hist

of 3.84e-5, a dropout rate of 0.15, 3 initial CNN kernel layers (dimension 384), 4 cross-attention layers (dimension 2048), and a shared prediction head (dimension 1024) in the end. The classifier reached 0.64 Spearman’s correlation score on validation data.

E.3 HALF-LIFE SCORE MODEL

Dataset Curation. The half-life dataset is curated from three publicly available datasets: PEPLife, PepTherDia, and THPdb2 (Mathur et al., 2016; D’Aloisio et al., 2021; Jain et al., 2024). Data related to human subjects were selected, and entries with missing half-life values were excluded. After removing duplicates, the final dataset consists of 105 entries.

Pre-training on stability data. Given the small size of the half-life dataset, which is insufficient for training a model to capture the underlying data distribution, we first pre-trained a score model on a larger stability dataset to predict peptide stability (Tsuboyama et al., 2023). The model consists of three linear layers with ReLU activation functions, and a dropout rate of 0.3 was applied. The model was trained on a 2xH100 NVIDIA NVL GPU system with 94 GB of VRAM for 50 epochs. The Adam optimizer was employed with a learning rate of 1e-2. A learning rate scheduler with 5 warm-up epochs and cosine decay was used, with initial and minimum learning rates both 1e-3. After training, the model achieved a validation Spearman’s correlation of 0.7915 and an R^2 value of 0.6864, demonstrating the reliability of the stability score model.

Fine-tuning on half-life data. The pre-trained stability score model was subsequently fine-tuned on the half-life dataset. Since half-life values span a wide range, the model was adapted to predict the base-10 logarithm of the half-life (h) values to stabilize the learning process. After fine-tuning, the model achieved a validation Spearman’s correlation of 0.8581 and an R^2 value of 0.5977.

F SAMPLING DETAILS

Score Model Settings. We cap the predicted log-scale half-life at 2 (i.e., 100 h) to prevent it from dominating the optimization and ensure balanced trade-offs across all properties. For the remaining objectives, hemolysis, non-fouling, solubility, and binding affinity, we directly employ their model outputs during sampling.

Wild-Type Peptide Binder Generation Task Settings. The total sampling steps are set to 20 multiplied by the binder length. All possible candidate token transitions are evaluated during each sampling step. We applied the same weight for each objective in all wild-type peptide binder generation tasks.

Chemically-Modified Peptide Binder Generation Task Settings. The total sampling steps are set to 128. With a vocabulary size of 586, evaluating all the possible candidate tokens is too computationally intensive. We therefore only evaluated the top 200 candidate tokens during each sampling step. We applied weight 0.7 for binding affinity, and 0.1 for hemolysis, non-fouling, and

1134 Table 4: Training and validation performance of PepReDi over successive rectification rounds. Each row reports
 1135 the training loss, validation negative log-likelihood (NLL), validation perplexity (PPL), and conditional total
 1136 correlation (TC). PepReDi without superscript denotes the base model, while PepReDi¹, PepReDi², PepReDi³
 1137 indicate the first, second, and third rounds of rectification, respectively.

	Train Loss	Val NLL	Val PPL	Conditional TC
PepReDi	1.6567	1.6458	5.19	10.6027
PepReDi ¹	1.6170	1.6101	5.00	12.6250
PepReDi ²	1.5347	1.5238	4.59	11.7279
PepReDi ³	1.3538	1.3548	3.88	11.2339

1146
 1147 solubility, respectively. Instead of random initialization, the initial sequences x_0 are sampled from
 1148 the pre-trained SMILESReDi¹ with 16 generation steps. During generation, AReUReDi rejects any
 1149 transitions that will make the SMILES sequence an invalid peptide.

G ABLATION STUDIES

1150
 1151 **Computational Cost.** We performed an ablation to study how AReUReDi’s performance scales
 1152 with the number of generation steps (Table 12). For wild-type binder design (MYC, 12-mers) and
 1153 chemically-modified binder SMILES design (NCAM1, length 200), we generated 100 binders using
 1154 64, 128, and 256 sampling steps. In both tasks, all optimized properties consistently improve as the
 1155 number of steps increases, while runtime grows approximately linearly with the step budget. However,
 1156 for NCAM1 the marginal gains in property scores from 128 to 256 steps are small compared to the
 1157 more than twofold increase in runtime. Based on this quality–compute trade-off, we use 128–256
 1158 steps for wild-type binder design tasks and 128 steps for chemically-modified binder design tasks in
 1159 the main experiments.

1160
 1161 **Weight Vectors.** To directly assess how AReUReDi explores the Pareto front, we ran experiments
 1162 on two three-objective tasks with varied Tchebycheff weights: wild-type peptide binder design for
 1163 CLK1 (Table 13) and chemically-modified peptide binder design for GFAP (Table 14). In
 1164 both cases, a balanced weight vector produces balanced improvements across all objectives, while
 1165 emphasizing a single objective systematically shifts the generated sequences toward that objective,
 1166 with corresponding trade-offs in the others. These results indicate that changing ω indeed steers
 1167 AReUReDi to different regions of the Pareto front rather than merely re-sampling the same trade-off
 1168 point.

1169
 1170 **ReDi Priors.** To directly assess the role of ReDi’s prior, we ran an ablation where we replaced the
 1171 ReDi prior $p_1(x)$ with a completely uninformed prior and kept the rest of AReUReDi unchanged,
 1172 across both wildtype binder (PPP5, 1B8Q) and chemically-modified binder (TfR, GLP1) design tasks.
 1173 In all cases, using the learned prior p_1 yields consistently better multi-objective performance. This
 1174 indicates that the discrete flow prior is not a redundant factor in the reward-tilted distribution, but a
 1175 crucial reference that anchors sampling in realistic, high-quality regions of sequence space, whereas
 1176 removing it degrades the quality of the discovered trade-offs.

1177
 1178
 1179
 1180
 1181
 1182
 1183
 1184
 1185
 1186
 1187

1188
1189
1190
1191
1192Table 5: Evaluation metrics for the generative quality of peptide SMILES sequences of max token length set to 200. SMILESReDi without superscription denotes the base model, while SMILESReDi¹ refers to the model that has undergone one round of rectification.1193
1194
1195
1196
1197
1198
1199
1200
1201
1202
1203
1204
1205

Model	Validity (↑)	Uniqueness (↑)	Diversity (↑)	SNN (↓)
Data	1.000	1.000	0.885	1.000
PepMDLM	0.450	1.000	0.705	0.513
SMILESReDi	0.763	1.000	0.719	0.593
SMILESReDi¹	0.986	1.000	0.665	0.579
PepTune	1.000	1.000	0.677	0.486
AReUReDi	1.000	1.000	0.789	0.392

1206
1207
1208
1209Table 6: **Adding a sampling constraint greatly improves AReUReDi’s performance.** Wild-type binders for two protein targets (PDB 8CN1 and 4EBP2) were generated with or without a sampling constraint using the same number of generation steps. The table reports the average score for each objective, calculated from 100 generated binders per setting. The best score for each objective is highlighted in bold.1210
1211
1212
1213
1214
1215
1216

Target	Method	Hemolysis	Non-Fouling	Solubility	Half-Life (h)	Affinity
8CN1	w/o constraints	0.8650	0.4782	0.4627	2.54	5.2412
	w/ constraints	0.9213	0.8676	0.8697	44.70	5.5143
4EBP2	w/o constraints	0.8879	0.4288	0.4257	1.8781	5.7132
	w/ constraints	0.9356	0.8767	0.8692	53.95	6.4571

1217
1218
1219
1220
1221
1222
1223

Table 7: Ablation results for wild-type peptide binder design targeting PDB 7LUL with different guidance settings. For each setting, 100 binders of length 7 were designed.

1224
1225
1226
1227
1228
1229
1230
1231
1232
1233
1234
1235
1236
1237
1238
1239
1240
1241

Guidance Settings			Hemolysis	Solubility	Affinity
Hemolysis	Solubility	Affinity			
✓	✓	✓	0.9389	0.9398	6.2559
✗	✓	✓	0.8964	0.9465	6.3272
✓	✗	✓	0.9502	0.4013	6.9798
✓	✓	✗	0.9535	0.9642	5.2611
✗	✗	✓	0.8812	0.2877	7.5057
✗	✓	✗	0.9036	0.9725	5.2449
✓	✗	✗	0.9802	0.6135	5.0985
✗	✗	✗	0.8431	0.5810	4.8919

1242
 1243 Table 8: Ablation results for wild-type peptide binder design targeting PDB CLK1 with different guidance
 1244 settings. For each setting, 100 binders of length 12 were designed.

Guidance Settings			Non-Fouling	Half-Life (h)	Affinity
Non-Fouling	Half-Life (h)	Affinity			
✓	✓	✓	0.8285	74.04	6.8099
✗	✓	✓	0.2902	96.59	7.3906
✓	✗	✓	0.9365	1.33	7.2029
✓	✓	✗	0.9479	75.68	6.3437
✗	✗	✓	0.9625	1.23	6.2319
✗	✓	✗	0.3540	100.00	6.4116
✓	✗	✗	0.2531	2.96	8.6580
✗	✗	✗	0.4988	1.82	5.4739

1263
 1264 Table 9: **Rectification of the base generation model improves AReUReDi’s performance.** Wild-type binders
 1265 for two protein targets (PDB 5AZ8 and AMHR2) were generated using AReUReDi with three different base
 1266 models: PepDFM, PepReDi (without rectification), and PepReDi³ (with three rounds of rectification). The table
 1267 reports the average score for each objective, calculated from 100 generated binders per setting. The best score
 1268 for each objective is highlighted in bold.

Target	Base Model	Hemolysis	Non-Fouling	Solubility	Half-Life (h)	Affinity
5AZ8	PepDFM	0.9296	0.8867	0.8743	37.30	6.2291
	PepReDi	0.9326	0.8759	0.8572	50.16	6.4391
	PepReDi ³	0.9293	0.8732	0.8605	58.33	6.2792
AMHR2	PepDFM	0.9412	0.8774	0.8612	47.84	7.2373
	PepReDi	0.9127	0.8602	0.8460	50.92	7.0101
	PepReDi ³	0.9420	0.8914	0.8755	63.34	7.2533

1278
 1279 Table 10: **Annealed guidance strength improves AReUReDi’s performance.** Wild-type binders for two protein
 1280 targets (PDB 1DDV and P53) were generated under four guidance schedules: (1) fixed at the minimum strength
 1281 $\eta_{min} = 1.0$, (2) fixed at the maximum strength $\eta_{max} = 20.0$, (3) fixed at the midpoint $\frac{1}{2}(\eta_{min} + \eta_{max}) = 10.5$,
 1282 and (4) an annealed schedule where η_t increases from η_{min} to η_{max} over optimization steps. The table reports
 1283 the average score for each objective, calculated from 100 generated binders per setting. The best score for each
 1284 objective is highlighted in bold.

Target	Method	Hemolysis	Non-Fouling	Solubility	Half-Life (h)	Affinity
1DDV	$\eta = \eta_{min}$	0.9130	0.8575	0.8429	38.70	5.3554
	$\eta = \eta_{max}$	0.9156	0.8512	0.8479	40.27	5.4359
	$\eta = \frac{1}{2}(\eta_{min} + \eta_{max})$	0.9108	0.8641	0.8544	40.43	5.5396
	$\eta_t = \eta_{min} + (\eta_{max} - \eta_{min}) \frac{t}{T-1}$	0.9128	0.8545	0.8565	44.73	5.4482
P53	$\eta = \eta_{min}$	0.9335	0.8800	0.8706	49.97	6.2538
	$\eta = \eta_{max}$	0.9293	0.8693	0.8657	61.76	6.3043
	$\eta = \frac{1}{2}(\eta_{min} + \eta_{max})$	0.9294	0.8713	0.8653	59.43	6.3060
	$\eta_t = \eta_{min} + (\eta_{max} - \eta_{min}) \frac{t}{T-1}$	0.9353	0.8818	0.8785	62.83	6.3508

1296
1297
1298
1299
1300
1301

Table 11: **Best-of- N comparison between PepTune+DPLM and AReUReDi under matched wall-clock time.** For each target, PepTune+DPLM is allowed to generate 100 binders while AReUReDi generates only 4 (PDB 1B8Q) or 3 (PPPS). Top-2 sequences from each method were reported. The table reports the average score for each objective.

1302
1303
1304
1305
1306
1307
1308
1309
1310
1311
1312
1313
1314

Target	Method	Rank	Hemolysis	Non-Fouling	Solubility	Half-Life (h)	Affinity
1B8Q	PepTune + DPLM	Top 1	0.9323	0.4379	0.3624	9.82	7.0534
		Top 2	0.8718	0.2573	0.2391	38.67	6.5605
	AReUReDi	Top 1	0.8651	0.8638	0.8892	100.00	5.6008
		Top 2	0.9354	0.8567	0.9331	49.25	6.5605
PPPS	PepTune + DPLM	Top 1	0.7984	0.3338	0.2342	80.27	7.6117
		Top 2	0.7901	0.0966	0.1328	100.00	6.7571
	AReUReDi	Top 1	0.9407	0.9378	0.9131	100.00	6.8193
		Top 2	0.9606	0.8750	0.8399	90.16	6.8969

1315
1316
1317
1318

Table 12: **Increasing generation steps improves AReUReDi’s performance.** AReUReDi designed 100 generated binders for MYC (12-mer wild-type peptides) and NCAM1 (chemically-modified peptides of length 200) using different numbers of generation steps. The table reports the average score for each objective. Half-life is not optimized for NCAM1 and is indicated by “*”.

1323
1324
1325
1326
1327
1328
1329
1330
1331
1332

Target	# Steps	Hemolysis	Non-Fouling	Solubility	Half-Life (h)	Affinity	Time
MYC	64	0.9279	0.8571	0.8519	5.49	6.5167	67
	128	0.9301	0.8721	0.8627	16.54	6.5811	131
	256	0.9357	0.8820	0.8740	34.83	6.5293	265
NCAM1	64	0.8801	0.2468	0.7954	*	5.3936	112
	128	0.8840	0.2657	0.8109	*	5.4377	198
	256	0.8900	0.3015	0.8202	*	5.5929	423

1333
1334
1335
1336

Table 13: Ablation results for wild-type peptide binder design targeting CLK1 with different weight vector settings. For each setting, 100 binders of length 12 were designed. The table reports the average score for each objective.

1340
1341
1342
1343
1344
1345
1346
1347
1348
1349

Weight Vectors			Non-Fouling	Half-Life (h)	Affinity
Non-Fouling	Half-Life	Affinity	Non-Fouling	Half-Life (h)	Affinity
0.3	0.3	0.3	0.8285	74.04	6.8099
0.8	0.1	0.1	0.9367	6.94	6.5231
0.1	0.8	0.1	0.5642	85.47	6.3649
0.1	0.1	0.8	0.6698	48.94	7.4922

1350
1351
1352
1353
1354
1355

Table 14: Ablation results for chemically-modified peptide binder design targeting GFAP with different weight vector settings. For each setting, 100 binders of length 200 were designed. The table reports the average score for each objective.

1356
1357
1358
1359
1360
1361
1362
1363
1364
1365
1366
1367
1368
1369
1370

Weight Vectors			Non-Fouling	Solubility	Affinity
Non-Fouling	Solubility	Affinity			
0.3	0.3	0.3	0.2754	0.8169	5.3011
0.8	0.1	0.1	0.3322	0.7528	5.3487
0.1	0.8	0.1	0.2273	0.8327	5.3378
0.1	0.1	0.8	0.2498	0.7910	5.8827

1371
1372
1373
1374Table 15: **PepReDi provides prior knowledge that helps AReUReDi to generate samples with better multi-objective trade-offs.** 100 wild-type binders were designed for PDB 1B8Q (8-mer) and PPP5 (16-mer), respectively. The table reports the average score for each objective. The best score for each objective is highlighted in bold.1375
1376
1377
1378
1379
1380
1381
1382
1383
1384
1385
1386
1387
1388
1389

Target	Prior	Hemolysis	Non-Fouling	Solubility	Half-Life (h)	Affinity
1B8Q	Uniform Prior	0.9009	0.8191	0.8049	14.20	5.8432
	PepReDi Prior	0.9214	0.8680	0.8654	22.93	5.7130
PPP5	Uniform Prior	0.9265	0.8263	0.7993	17.52	6.7122
	PepReDi Prior	0.9412	0.896	0.8832	38.28	6.7186

1390
1391
1392
1393
1394
1395
1396
1397
1398
1399
1400
1401
1402
1403Table 16: **SMILESReDi provides prior knowledge that helps AReUReDi to generate samples with better multi-objective trade-offs.** For each setting, 100 chemically-modified binders of length 200 were designed. The table reports the average score for each objective. The best score for each objective is highlighted in bold.

Target	Prior	Hemolysis	Non-Fouling	Solubility	Affinity
TfR	Uniform Prior	0.8652	0.2381	0.7777	5.5535
	SMILESReDi Prior	0.8665	0.3234	0.7408	6.1271
GLP1	Uniform Prior	8.3414	0.2123	0.7777	7.5731
	SMILESReDi Prior	0.8743	0.3438	0.7661	8.3414

1404

1405

1406

1407

1408

1409

1410

1411

1412

1413

1414

1415

1416

1417

1418

1419

1420

1421

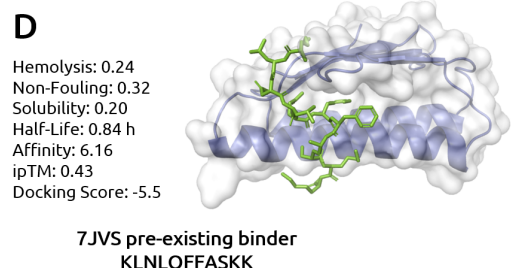
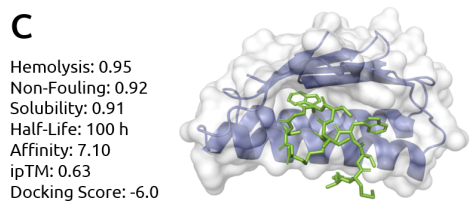
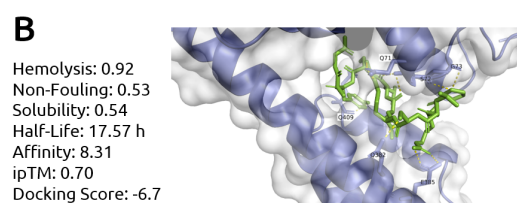
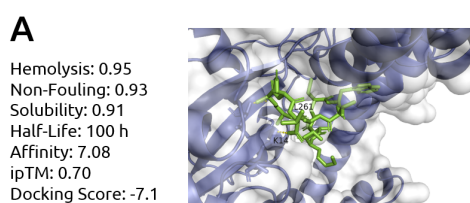


Figure A1: Complex structures of target proteins with pre-existing binders. (A)-(B) 5AZ8 (C)-(D) 7JVS. Each panel shows the complex structure of the target with either an AReUREDi-designed binder or its pre-existing binder. For each binder, five property scores are provided, as well as the ipTM score from AlphaFold3 and the docking score from AutoDock VINA. Interacting residues on the target are visualized.

1442

1443

1444

1445

1446

1447

1448

1449

1450

1451

1452

1453

1454

1455

1456

1457

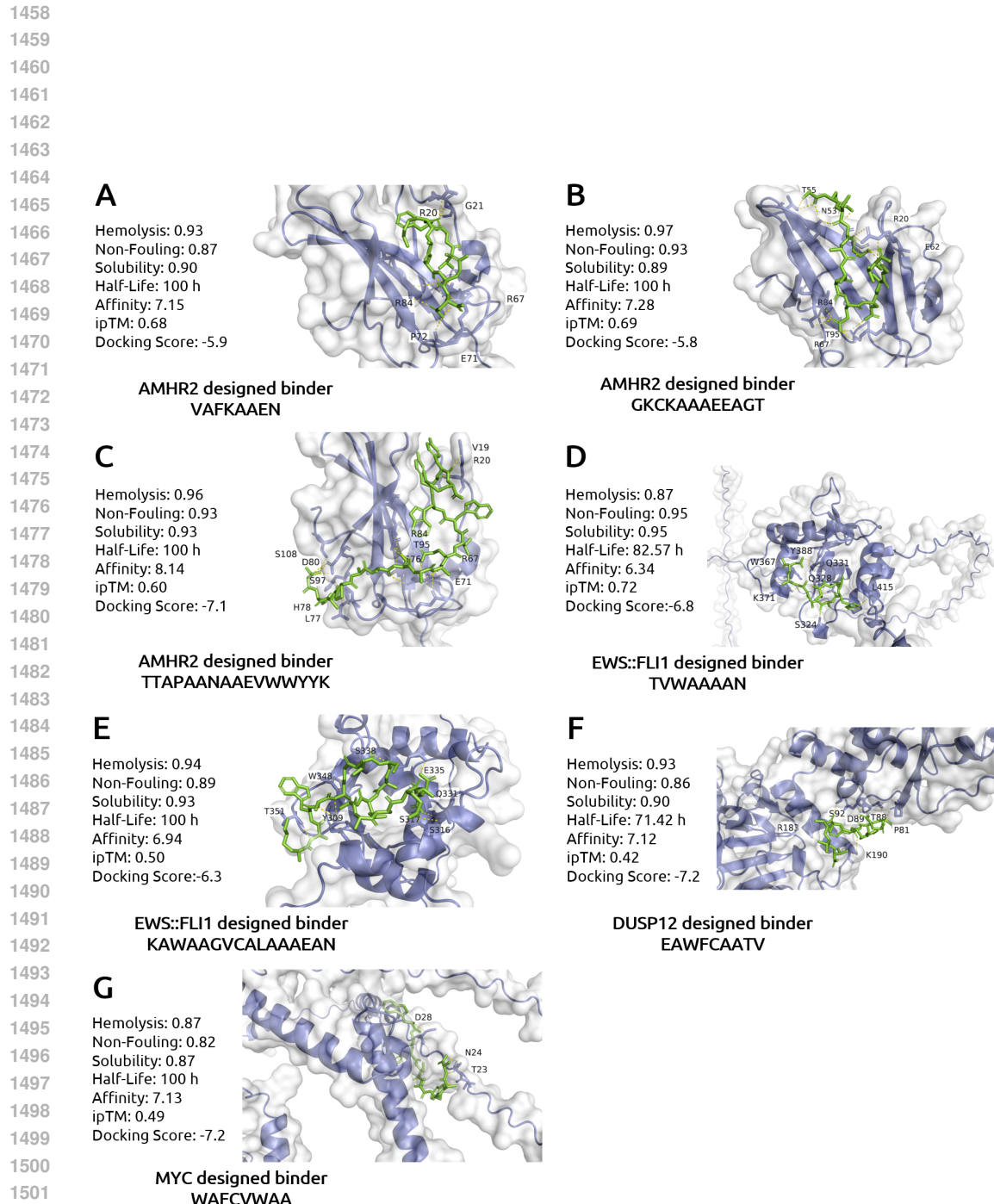


Figure A2: **Complex structures of target proteins without pre-existing binders.** (A)-(C) AMHR2, (D)-(E) EWS::FLI1, (F) MYC, (G) DUSP12. Each panel shows the complex structure of the target with an AReUReDi-designed binder. For each binder, five property scores are provided, as well as the ipTM score from AlphaFold3 and the docking score from AutoDock VINA. Interacting residues on the target are visualized.

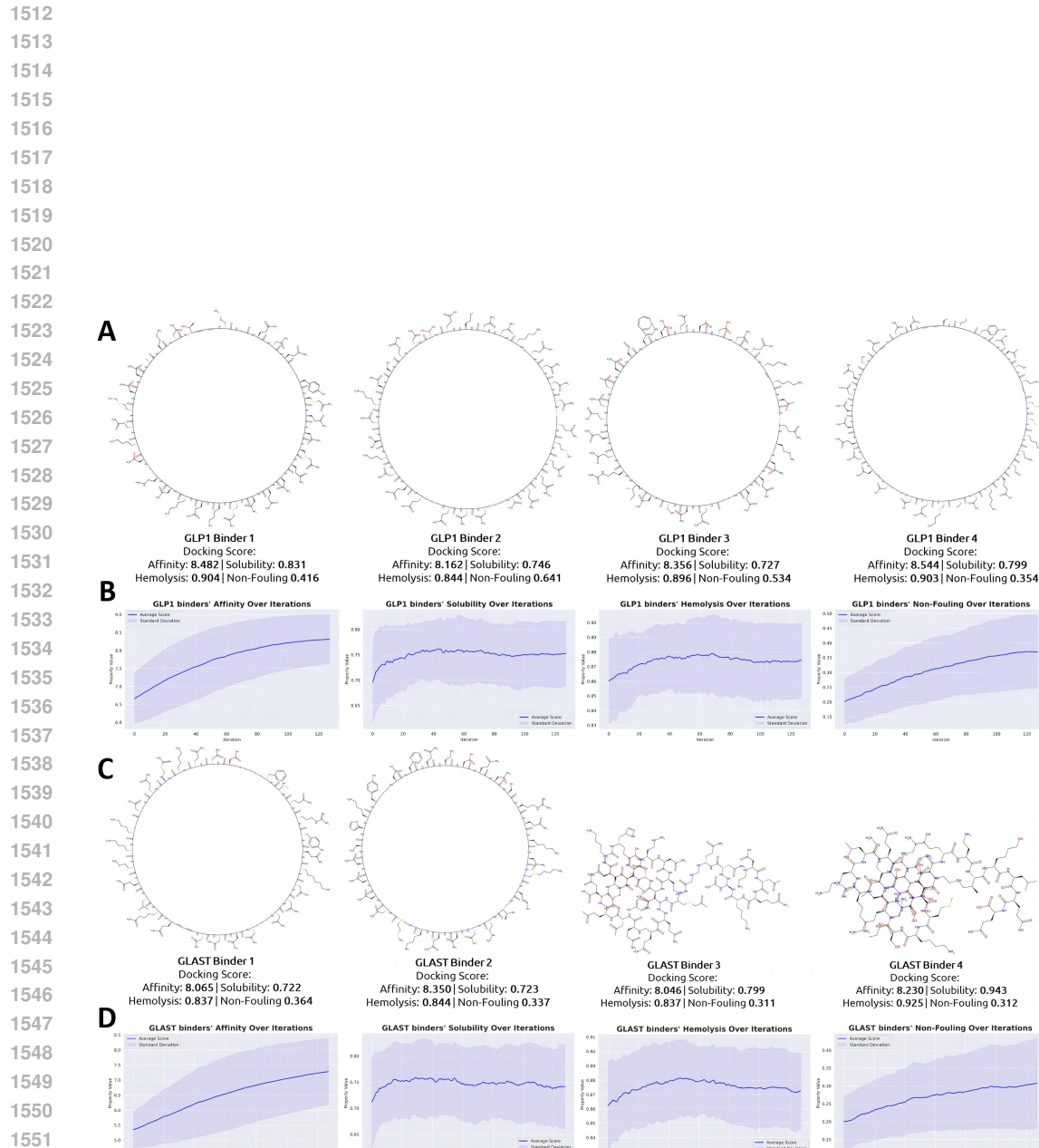


Figure A3: **(A), (C)** Example 2D SMILES structure of AReUReDi-designed peptide binders with four property scores for GLP1 and GLAST, respectively. **(B), (D)** Plots showing the mean scores for each property across the number of iterations during AReUReDi's design of binders of length 200 for GLP1 and GLAST, respectively.

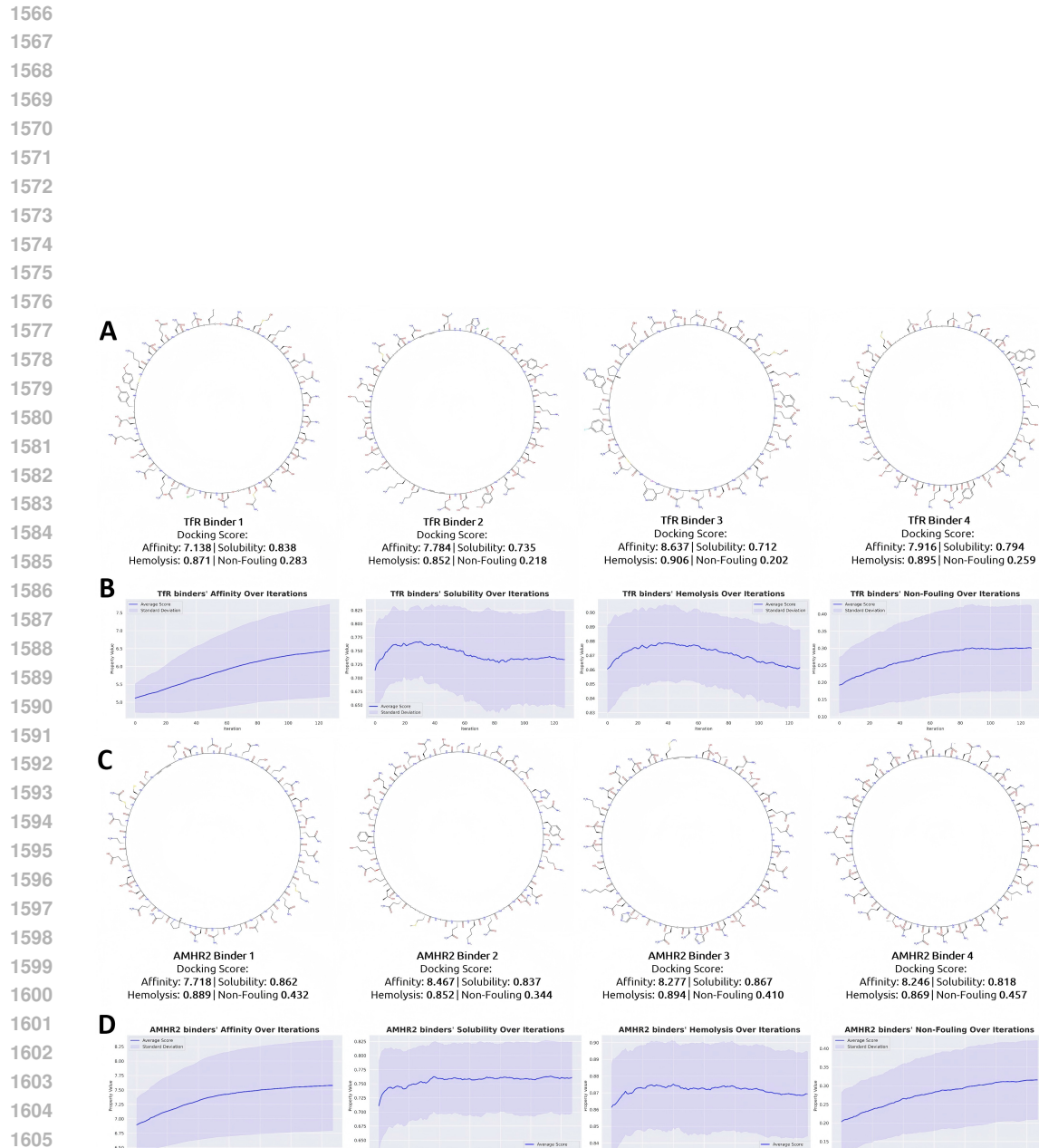


Figure A4: (A), (C) Example 2D SMILES structure of AReUReDi-designed peptide binders with four property scores for TfR and AMHR2, respectively. (B), (D) Plots showing the mean scores for each property across the number of iterations during AReUReDi's design of binders of length 200 for TfR and AMHR2, respectively.

1620 **Algorithm 1** AReUReDi: Annealed Rectified Updates for Refining Discrete Flows

1621 1: **Input:** Pre-trained ReDi model $p_t^i(\cdot|x_t)$, objective functions $\tilde{s}_1, \dots, \tilde{s}_N$, weight vector $\omega \in \Delta^{N-1}$, annealing parameters η_{min}, η_{max} .

1622 2: **Output:** Sequence x_T with multi-objective optimized properties.

1623 3: **Initialize:**

1624 4: Sample an initial sequence x_0 uniformly from the discrete state space S

1625 5: Sample or specify a weight vector $\omega \in \Delta^{N-1}$

1626 6: **for** $t = 0$ to 1 with step size $h = \frac{1}{T}$ **do**

1627 7: **Step 1: Annealing and Coordinate Selection**

1628 8: Update guidance strength: $\eta_t \leftarrow \eta_{min} + (\eta_{max} - \eta_{min}) \frac{t}{T-1}$

1629 9: Select a position i in the sequence to update: $i \sim \text{Uniform}(\{1, \dots, L\})$

1630 10: **Step 2: Proposal Generation via Local Balancing**

1631 11: Let C_i be the set of candidate tokens from $p_t^i(\cdot|x_t)$.

1632 12: For each candidate token $y \in C_i$:

1633 13: Compute scalarized reward ratio $r_i(y; x_t)$:

1634 14:
$$r_i(y; x_t) \leftarrow \frac{\exp(\eta_t \min_n \omega_n \tilde{s}_n(x^{(i \leftarrow y)}))}{\exp(\eta_t \min_n \omega_n \tilde{s}_n(x))}$$

1635 14: Compute unnormalized proposal distribution $\tilde{q}_i(y|x_t)$ using a balancing function $g(\cdot)$:

1636 15:
$$\tilde{q}_i(y|x_t) \leftarrow p_t^i(y|x_t) g(r_i(y; x_t))$$

1637 15: Normalize to get the final proposal distribution $q_i(y|x_t)$.

1638 16: **Step 3: Metropolis-Hastings Acceptance**

1639 17: Sample a candidate token $y^* \sim q_i(\cdot|x_t)$.

1640 18: Form the proposed state $x_{prop} \leftarrow x^{(i \leftarrow y^*)}$.

1641 19: Compute acceptance probability $\alpha_i(x, x_{prop})$:

1642 14:
$$\alpha_i(x, x_{prop}) \leftarrow \min \left\{ 1, \frac{\pi_{\eta_t, \omega}(x_{prop}) q_i(x^i|x_{prop})}{\pi_{\eta_t, \omega}(x) q_i(y^*|x)} \right\} \quad \pi_{\eta_t, \omega}(z) \propto p_1(z) \exp(\eta_t \min_n \omega_n \tilde{s}_n(z))$$

1643 20: With probability $\alpha_i(x, x_{prop})$, accept the proposal: $x \leftarrow x_{prop}$.

1644 21: Update time: $t \rightarrow t + h$

1645 22: **end for**

1646 23: **Return:** Final sequence x_1 .

1652

1653

1654

1655

1656

1657

1658

1659

1660

1661

1662

1663

1664

1665

1666

1667

1668

1669

1670

1671

1672

1673

1674 **H USE OF LARGE LANGUAGE MODELS (LLMs)**
16751676 We acknowledge the use of large language models (LLMs) to assist in polishing and editing parts of
1677 this manuscript. LLMs were used to refine phrasing, improve clarity, and ensure consistency of style
1678 across sections. All technical content, experiments, analyses, and conclusions were developed by the
1679 authors, with LLM support limited to language refinement and editorial improvements.
1680

1681

1682

1683

1684

1685

1686

1687

1688

1689

1690

1691

1692

1693

1694

1695

1696

1697

1698

1699

1700

1701

1702

1703

1704

1705

1706

1707

1708

1709

1710

1711

1712

1713

1714

1715

1716

1717

1718

1719

1720

1721

1722

1723

1724

1725

1726

1727